

Details of the research work duly signed by the applicant, for which the Sun Pharma Research Fellowship is claimed, including references and illustrations (not to exceed 6000 words).

My lab has attained a significant place in developing innovative functionalized nano-biomaterials for therapeutic & and diagnostic applications and elucidating the mechanistic aspect of its cellular translocation to achieve a higher therapeutic index with low toxicity of drugs. My focus signifies a major role in establishing specific delivery of drugs through innovative nano-therapeutics thereby bypassing the otherwise established biological barriers. My contribution lies basically in two verticals i.e. (a) Knowledge generation and development and (b) Translational Contribution and commercialization. In the segment **Knowledge generation and development**, we have explored different mechanisms like *ligand-receptor interactions*, *endosomal pH responsiveness* and *receptor-mediated endocytosis* and its link to *cancer nano-therapeutics*. This led to high-impact publications in the journals of repute. In the other segment **Translational contribution and commercialization**, we have successfully developed layer-by-layer (LBL) and SMEDDS technology that impacted product development in the area of bone-related disorders. We have been instrumental in patenting 25 technologies, out of which FIVE have been licensed to Industries while TWO are commercialized as **Joint Fresh™** and **Reunion™** [(Granted US patent 8,496,964; AU Patent; 2010217238A; EP patent 2400957 B1) Other products for the treatment of osteoarthritis and bone loss are also developed (Granted US Patent 10,596,115; AU Patent 2014291615; US patent 10265297)]. In addition, he has been actively involved in developing Umifenovir and its formulation under repurposing for COVID patients whose Phase III clinical trial has been completed.

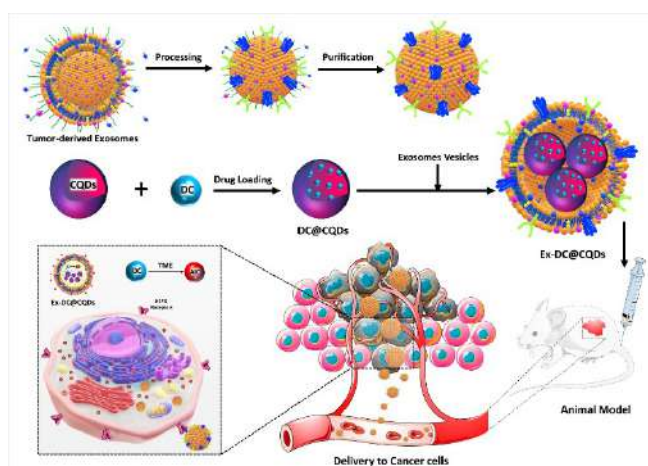
[A] KNOWLEDGE GENERATION AND DEVELOPMENT: The focus of our research involves engineering biomaterials to explore niche areas of translational research and establish specific delivery of drugs through innovative nano-therapeutics thereby bypassing the otherwise established biological barriers. We have discovered that breast cancer cell derived exosomes facilitates receptor mediated fusion & intracellular trafficking of quantum dots resulting spatial targeting to tumors at significantly lower dose. In addition, the development of multifunctional nanoparticles for synchronized imaging and tumor-targeted non-invasive therapy through optical imaging is supposed to have a notable impact on future personalized oncology. In this segment, we have established the role of ***comprehensive nano-theranostics*** with detailed mechanistic understanding that play a pivotal role in rationalizing therapeutic strategy for cancer. We have elucidated Aggregation Induced Emission mechanism demonstrating image-guided chemotherapy through anisamide and Mn²⁺ functionalized inverse hexagonal particles. He also established proton sponge effect escaping lysosomal degradation by pyridoxine tethered nanoparticles facilitating intracellular localization while modulation of tumor microenvironment using endogenous stimuli-responsive lyotropic nano-liquid crystals ensuing patient-friendly comprehensive cancer nano-theranostics. The detailed strategies discussed in the current context are as follows.



[a] Dacarbazine-primed carbon quantum dots coated with breast cancer cell-derived exosomes for improved breast cancer therapy [J. Controlled Rel. 365; 43-59 (2024)]

Exosomes have emerged as a promising strategy for drug delivery in cancer treatment due to their unique properties. These small extracellular vesicles, ranging from 30 to 150 nanometers in diameter, are naturally released by cells and play a key role in cell-to-cell communication. Their ability to transfer bioactive molecules such as proteins, lipids, and nucleic acids makes them an attractive vehicle for delivering therapeutic agents to target cells, particularly in the context of cancer. Exosomes have intrinsic targeting abilities, as they carry surface proteins and lipids that can recognize and bind to specific receptors overexpressed in tumor tissues.

In this line we developed a strategy for targeted delivery of Dacarbazine (DC) to breast cancer (BC) cells using Exosome (Exo) coated carbon quantum dots (CQDs). DC was loaded onto CQDs to improve its solubility and photostability and then encapsulated within cell derived Exosomes (Exo) derived from BC cells (Ex-DC@CQDs) for therapeutic targeting. Exo can selectively target cancer cells through HSPG receptors and safeguard the integrity of DC and CQDs [Barbouri *et al*, 2014]. Exo expedite the conveyance of DC@CQDs to cancer cells by fusing with the cell membrane and facilitating the activation of DC specifically within cancer cells. Exo released by BC cells contain specific proteins (heparanase, syndecan-1, and glypican-1) that bind to HSPG receptors, accenting the involvement of the receptor in essential cellular processes. The interaction between Exo and HSPG receptors triggers an internalization process mediated by endocytosis [Christianson *et al* 2013]. This enables efficient delivery of exosomal cargo, including drugs and macromolecules to the target cells, ensuring a targeted therapeutic approach. In addition, Exo isolated from BC cells are innately endowed with the capacity to express these vital cytochrome enzymes, which will facilitate activation of DC, negating the prerequisite for enzyme presence on the surface of cancer cells.



Bohe

Dacarbazine (DC) is a chemotherapy prodrug that exerts its anticancer effects through a multifaceted mode of action. Once administered, DC is metabolically activated in the

liver, forming reactive metabolites that bind covalently to DNA molecules in cancer cells. Challenges in its application to BC treatment arise from its poor aqueous solubility, susceptibility to photodegradation, and short biological half-life. These limitations can affect drug distribution, bioavailability, and treatment efficacy, and may lead to non-specific cytotoxic effects on healthy cells and adverse side effects [Al-Badr and Alodhaib 2016; Tagne 2008].

Therefore, it was hypothesized that cytochrome enzymes, particularly CYP1A1, CYP1A2, and CYP2E1, being integral parts of the Exo would facilitate direct activation of DC within the tumor microenvironment (TME) after HSPG-mediated spatial targeting of Ex-DC@CQDs into tumor cells, thereby engendering improved efficacy while minimizing untoward effects on normal cells [Christianson *et al* 2013]. Thus, Exo co-loaded with CQDs and DC can provide significant therapeutic effects against BC while avoiding the many risks associated with the free DC. Moreover, Exo possess an intrinsic ability to cross biological barriers, enabling them to encounter the phagocytosed drug lost during circulation.

Fucose-in-water-and-PE-PEG-based CQDs were developed and optimized by slightly modifying the reported method [Choi *et al* 2017; Medeiros *et al* 2019]. The optimized CQDs were then selected and further incubated with DC to successfully load the drug, resulting in the development of DC@CQDs [Zeng *et al* 2016]. Afterward, the DC@CQDs were effectively loaded into isolated and purified Exo using a previously reported method, leading to the formation of Ex-DC@CQDs [Rao *et al* 2019; Sun *et al* 2019]. The DC@CQDs exhibited a size range of 2-10 nm (Average particle size, APS, 8.25 ± 0.23 nm; PDI 0.21 ± 0.05), which was suitable for their loading into extracellular vesicles [Rao *et al* 2019; Sun *et al* 2019]. However, the size of the Exo was slightly higher (50-300 nm, Figure 1A, C); consequently, the APS for the final formulation (Ex-DC@CQDs) (APS, 110.70 ± 10.0 nm; PDI 0.18 ± 0.09) increased (Figure 1G). Nanocarriers within the size range of 50-300 nm are known to have improved localization at the tumor site, benefiting from the enhanced permeability and retention (EPR) effect [Sharifi *et al* 2022]. Moreover, the surface potentials of DC@CQDs and Ex-DC@CQDs were measured to be -26.7 ± 7.73 mV and -34.6 ± 6.41 mV, respectively, indicating promising stability of the dispersion system and suitability for IV administration [Rasmussen *et al* 2020]. The hydrodynamic particle sizing through NTA in each milliliter formulation dispersion (Ex-DC@CQDs) ensured an overall Exo diameter <100 nm; however, the number of Exo between 100 and 300 nm was low (Figure 1B). Further, it is essential that Exo retain all their structural and functional characteristics after being extracted from the parent cell to carry out their function as tumor cell targets. The Exo formulation (Ex-DC@CQDs) exhibited expressions of their specific markers, including CD81, CD63, CYP2E1, CYP1A1, and CYP1A2, in Western blotting (Figure 1K) [Wang *et al* 2022]. The significant levels of expression of these proteins were observed in the isolated Exo and in the Ex-DC@CQDs. Also, the protein expression of CYP1A1, CYP1A2, CYP2E1 in Ex-DC@CQDs ensured the site-specific conversion of DC into an active form under favorable TME, suggesting that Exo may serve as delivery vehicles with structural and

functional integrity. The photoluminescence (PL) properties of quantum dots are attributed to their component and respective functional groups that play a vital role in overall features [Papaioannou *et al* 2018]. When exposed to light, aromatic compounds undergo distinct excitation and relaxation processes, resulting in the emission of fluorescence. The presence of aromatic hydroxyl groups on the surface of quantum dots establishes an abundance of π -electron systems, serving as fluorescent centers. These centers proficiently absorb excitation energy and subsequently release light, yielding fluorescence.

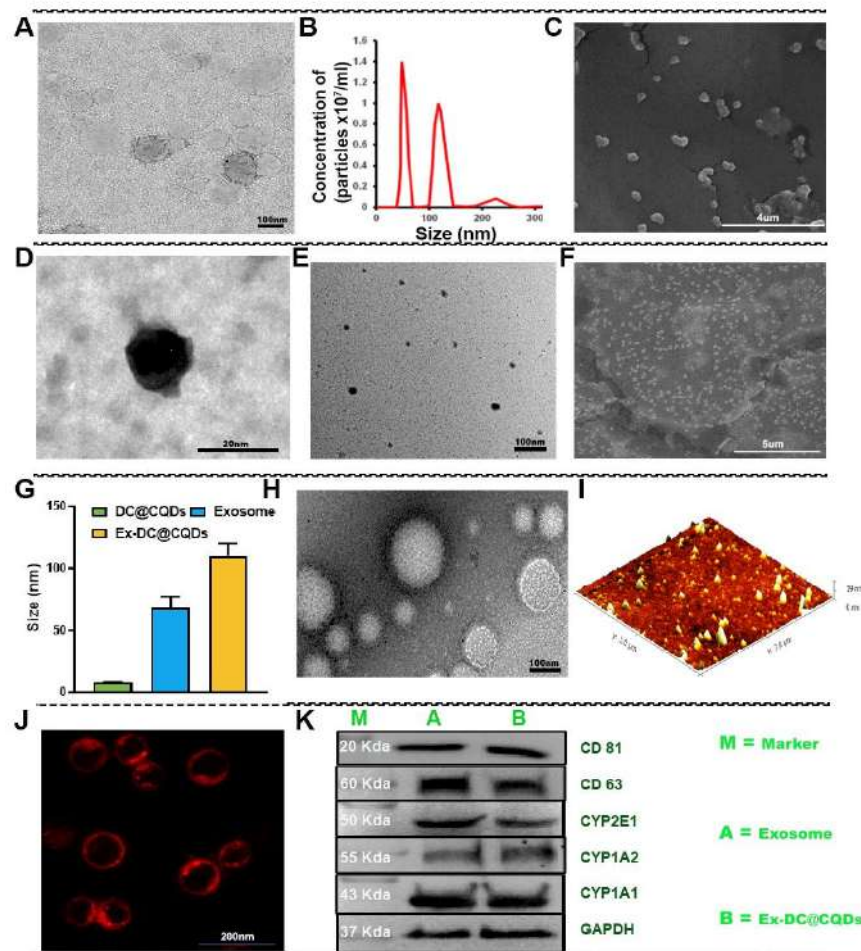


Figure 1. Morphological and surface characterization. (A) Characterization of MD-MB-468 isolated Exo by TEM image. (B) Size characteristic and intensity of Exo through NTA. (C) SEM image of Exo. (D) TEM image of synthesized DC@CQDs. (E) HR-TEM image of DC@CQDs. (F) SEM image of DC@CQDs. (G) The relative particle size of developed formulation. (H) TEM image of Ex-DC@CQDs. (I) 3D AFM image of DC@CQDs. (J) Confocal based characteristic presence of HSPG protein following staining with syndican1 antibody on Exo. (K) Characteristic presence of marker of Exo exploration by Western blot analysis. All the data were present as n=3.

The UV-vis absorption spectrum of quantum dots exhibits a pronounced capacity for light absorption at a specific wavelength of approximately 326 nm (Figure 2A). This absorption phenomenon can be attributed to the presence of distinctive chemical bonds within the quantum dots, namely the aromatic C=C bond and the sp² system housing C=O and C=N bonds. When these bonds capture light, a π - π^* or n- π^* transition occurs, triggering vibrations and the subsequent emission of light at an altered wavelength [Papaioannou *et al* 2018]. Markedly, the emission of bright blue

fluorescence emerges when quantum dots are excited with UV light at 366 nm, owing to these reported transitions. The optimal excitation wavelength for fluorescence detection in the context of quantum dots was determined to be 488 nm (Figure 2B). The release of DC from Ex-DC@CQDs is depicted in Figure 2 at pH 5.5 and 7.4. Ex-DC@CQDs demonstrated the release of approximately 60% of the DC in 24 h at pH 5.5; however, when the pH was 7.4, only 40% of the drug was released under the same conditions. The release of DC from Ex-DC@CQDs was considerably faster in an acidic environment, corresponding to TME, and significantly slower at a pH of 7.4, corresponding to the remaining and more abundant physiological pH in the body. The cumulative DC release from Ex-DC@CQDs was 1.5 times- higher at pH 5.5 than at pH 7.4. Further, the stability of Ex-DC@CQDs was monitored in PBS at 4°C for one month (pH 7.4).

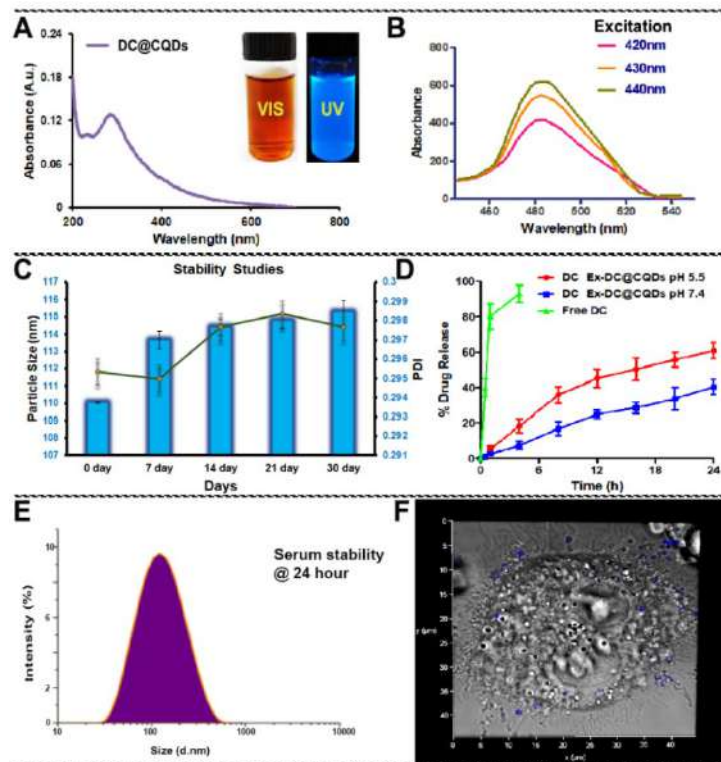


Figure 2. (A, B) Fluorescent photograph and spectrum of DC@CQDs upon UV illumination (366 nm). (C) The physical stability of the Ex-DC@CQDs. (D) % Drug release from Ex-DC@CQDs at pH 7.4 and 5.5. (E) Serum stability study of Ex-DC@CQDs. (F) 3D confocal microscopic imaging of particle internalization (DC@CQDs) in the MDA-MB-231 cell line. All the data were recorded (n=3).

The cellular uptake of the developed formulation (DC@CQDs and Ex-DC@CQDs) through the HSPG receptor was examined using CLSM and flow cytometry techniques. The CSLM results revealed that the targeted formulation's fluorescence intensity was initially found in the cytoplasm and nucleus regions of the cells within 2 h, and subsequently diffused into the nucleus over the next 6 h. Additionally, the enhanced accumulation of Ex-DC@CQDs in the cytoplasm was observed through differential fluorescence intensity, which can be attributed to the HSPG protein on the formulation's surface, acting as a targeting motif that complements the HSPG surface receptor (Figure 1J). MDA-MB-231 cells were exposed to DC@CQDs (without any cellular fluorescent dye) for 6 h, and the results demonstrated clear internalization of

Ex-DC@CQDs, showing a blue-colored spot corresponding to the auto-fluorescent emission of CQDs on the outer surface of the cell. However, after internalization, the spot appeared dull, greyish, and silvery due to the cell membrane covering, confirming the effective internalization of DC@CQDs (Figure 2F). Moreover, it is known that cancer cells possess HSPG-specific receptors, and Exo with HSPG protein preferentially interacts with these receptors, triggering receptor-mediated endocytosis in these cells [Gonda *et al* 2019]. To confirm that Ex-DC@CQDs undergo receptor-mediated endocytosis, a receptor-blocking study was conducted. Highly metastatic cell lines, such as MDA-MB-231 and 4T1, which express a higher level of HSPG receptors on their cell surface, were used for this study. The cells were pre-treated with 1 μ M integrin antibody to saturate the receptors [Rennick *et al* 2021], and then both the non-targeted (DC@CQDs) and Exo-encapsulated (Ex-DC@CQDs) formulations were treated to demonstrate and validate the role of HSPG receptors in endocytosis. Subsequently (Figure 3, D-E), it was observed that after 6 h of treatment, the average fluorescence intensities of both formulations were almost identical, indicating that the interaction between HSPG and the HSPG receptor played a crucial role in enhancing cellular uptake inside the cells.

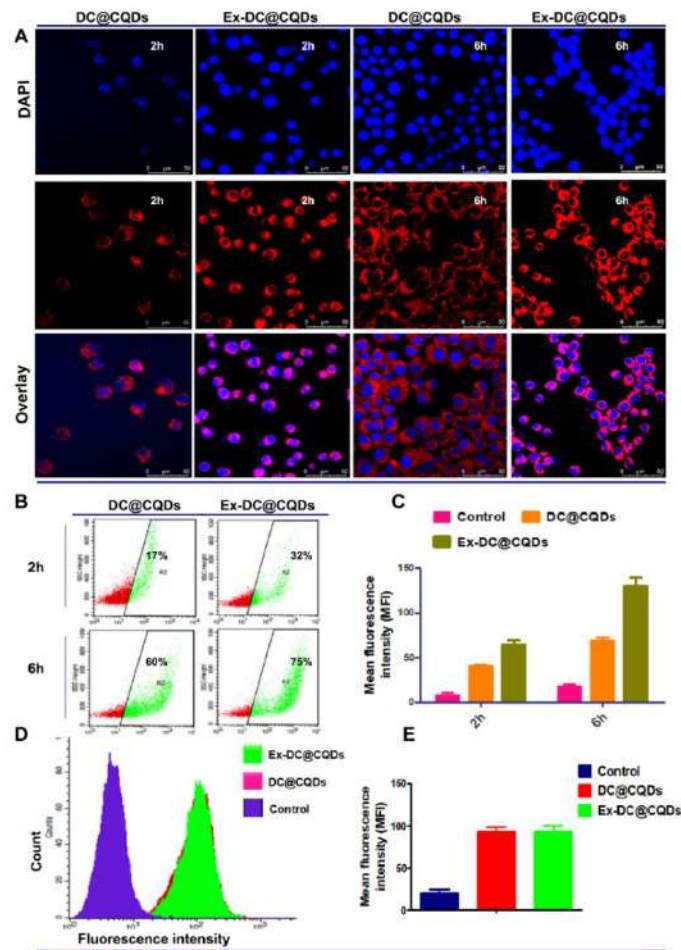


Figure 3. (A-C) The qualitative and quantitative assessments of Nile red-tagged Exo encapsulated formulation (Nile Red- DC@CQDs and Ex-DC@CQDs) after 2 and 6 h treatment of MDA-MB-231 cells using confocal microscopy. (B) Flow cytometry-based quantitative estimation of the cellular uptake in MDA-MB-231 cells following incubation for 2 and 6 h. (D-E) Receptor blocking study in MDA-MB-231 cells. All the experiments were achieved in triplicate (n=3).

Blue

Cell cycle arrest, apoptosis, and MMP were examined using flow cytometry to compare the effects of DC in its free form and as a formulation within Exo. DC is an anticancer drug that has been extensively studied for its ability to halt cancer cells in the G1 or S phase. MDA-MB-231 cells treated with Ex-DC@CQDs exhibited a higher degree of apoptosis in the cancer cell population compared to non-targeted DC@CQDs and free drug, which was significantly corroborated with the outcomes from cell cycle arrest. Treatment with free DC and CQDs showed almost $19.8 \pm 2.3\%$ and $14.5 \pm 1.8\%$ apoptosis, respectively (Figure 5B and E). However, a total of $65.5\% \pm 7.5\%$ apoptotic population comprising early and late apoptosis was seen following treatment with Ex-DC@CQDs. In addition to this, it was noticed that the DC@CQDs had an added effect on the enhancement of DC sensitivity. Also, the depolarization of the mitochondrial membrane was observed in $13 \pm 2.5\%$ and $10 \pm 2.1\%$ of the cell population by free DC and CQDs, respectively. The non-targeted therapy merely increased depolarization by $39 \pm 3.5\%$; however, Ex-DC@CQDs showed a cumulative $57 \pm 7.1\%$ increase in depolarization relative to the other treatment groups (Figure 5A and D). Altogether, these outcomes indicate that CQDs may significantly enhance the sensitivity of DC as a free drug or in Exo formulation, apparently via cell cycle arrest and synergistic mitochondrial depolarization leading to higher apoptosis.

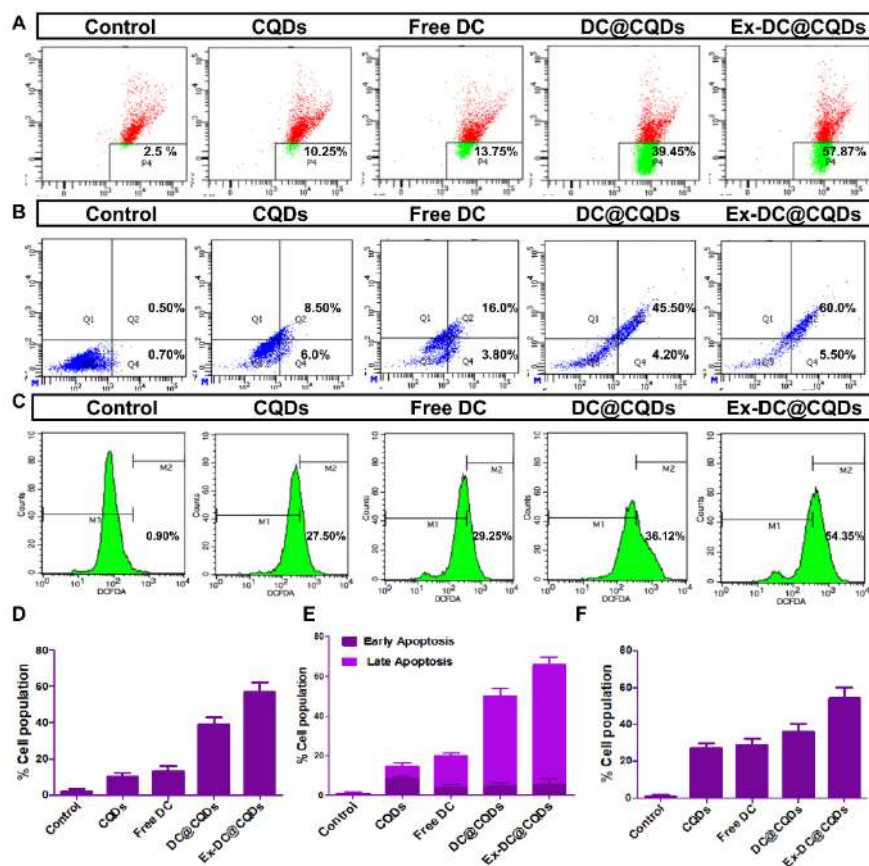


Figure 5. Flow cytometry data for MMP, apoptosis, and ROS in the MDA-MB-231 cell line. (A and D) Representative % depolarization of MMP after 48 h of treatment. (B and E) Results in early and late apoptosis in MDA-MB-231 cells following 48 h of incubation. (C and F) ROS generation after 48 h of treatment. These results were obtained in triplicate (n = 3) mean SD.

Signature

To investigate the bio-distribution of Ex-DC@CQDs at the tumor site, Balb/c tumor-bearing mice induced with 4T1 cells were administered Evans blue dye (Near-Infrared) labeled Ex-DC@CQDs and DC@CQDs [Salunkhe *et al* 2020]. This administration took place after the tumors had reached a volume of 200 to 300 mm³. In order to track the distribution of the developed formulation, IVIS imaging was performed at designated time points before and after IV administration of formulation containing DC equivalent to 10 mg/kg, along with Evans-labeled Ex-DC@CQDs and DC@CQDs. Fluorescence images of the mice were captured at different time intervals (6, 12, and 24 h), and the deposition of Ex-DC@CQDs at the tumor site was assessed by quantifying the fluorescence intensity within a defined region of interest.

After 12 h of injection, a significant and sustained increase in fluorescence intensity was observed in the Exo-specific HSPG receptor targeted group (Ex-DC@CQDs) at the tumor site, which remained consistent for up to 24 h (Figure 6, A-B). This finding highlights the superior localization of the Exo-specific HSPG receptor-targeted group (Ex-DC@CQDs) in the tumor tissue compared to the DC@CQDs groups. The effectiveness of the targeted formulation in achieving specific illumination of tumor tissue with a significant contrast can be attributed to the internalization process mediated by Exo and driven by the HSPG receptors [Zhang *et al* 2023]. In contrast, the relatively weak fluorescence observed at the tumor site for non-targeted nanoparticles (DC@CQDs) and the higher fluorescence signal in other organs can be attributed to their lack of targeting capability and systemic distribution [Li *et al* 2020]. Furthermore, the confirmation of these findings was obtained through *ex vivo* imaging of the tumor tissue and major organs collected from the sacrificed animals 24 h post-injection. The investigation of fluorescence intensity differences between the groups treated with targeted and non-targeted formulations was conducted by analyzing the differential distribution of formulation. Additionally, it was also found that the non-targeted group had a higher fluorescence intensity in the liver tissue than the targeted group, which indicates that the targeted formulation demonstrated an extended duration of circulation in the bloodstream and the target-specific drug delivery at the tumor site (Figure 6, C-E). The aforementioned results were consistent with the outcomes of our *In vivo* pharmacokinetic study, providing further confirmation. Thus, Ex-DC@CQDs have been proven to have the ability to target the TME in which overexpressed cancer-derived Exo-specific receptors are present.



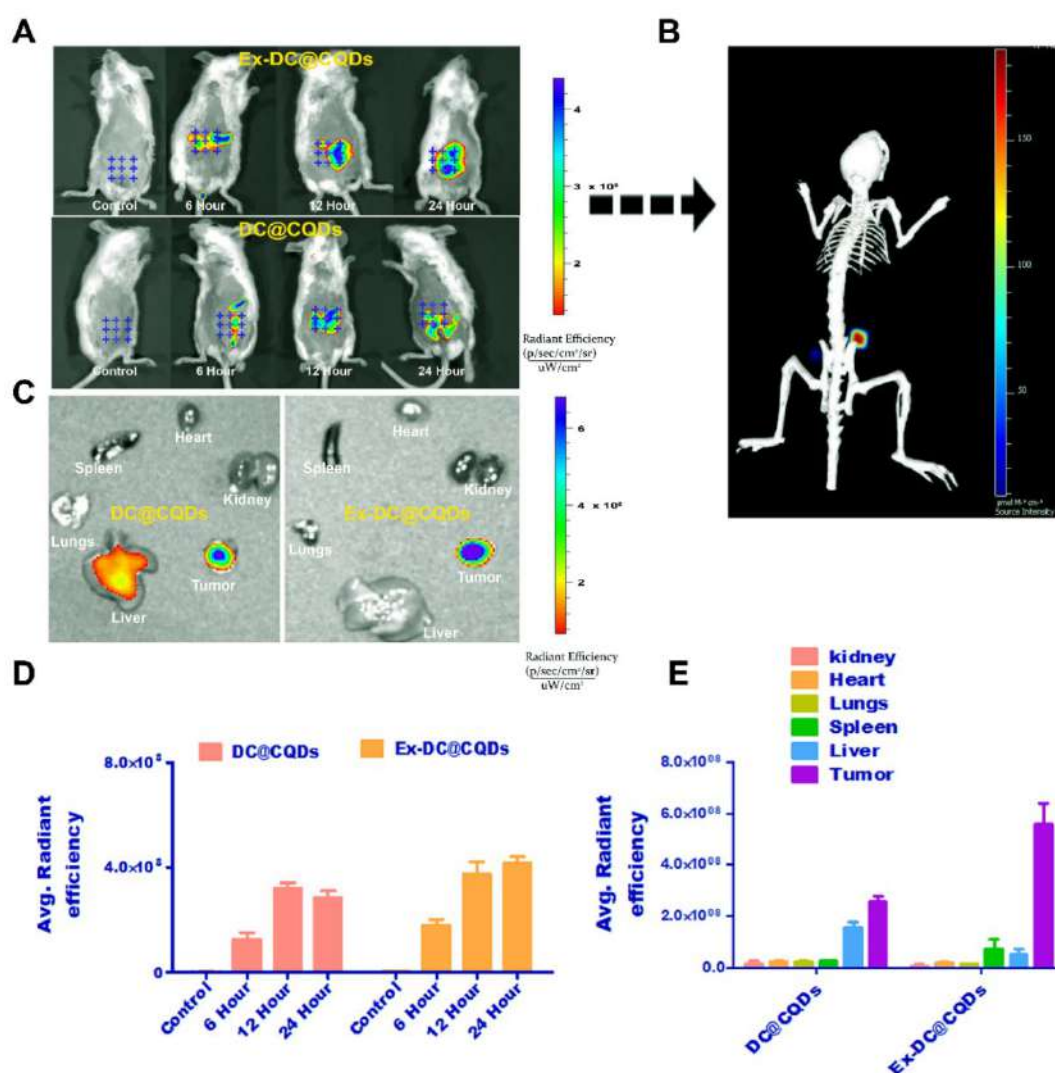


Figure 6. Visualization of *In vivo* imaging and tumor-targeting study after IV administration of Evans blue-labeled developed formulation. (A) Whole-body image comparing targeted and non-targeted groups. (B) Three-dimensional *In vivo* imaging model. (C) Ex vivo imaging of vital organs from the same experimental setup. (D) Quantitative assessment of the fluorescence intensity specific to tumors in groups of animals treated with Ex-DC@CQDs and DC@CQDs formulations. (E) *Ex vivo* quantitative assessment of fluorescence signals in vital organs. All data are expressed as mean \pm standard deviation ($n = 3$).

To study the effect of Ex-DC@CQDs on the pharmacokinetics and biodistribution of DC, mice with tumors were administered free DC, DC@CQDs, and Ex-DC@CQDs via IV injection at a dose of 10 mg/kg through the tail vein. The serum distribution profile over 24 h is presented in Figure 7, panels A and B. the administration of DC encapsulated in CQDs resulted in a distinct profile in both organs and serum over a 24 h period, differing from that of free drugs alone. Notably, the groups treated with Ex-DC@CQDs exhibited substantial increases in AUC_{0-∞} compared to both free DC and DC@CQDs. Specifically, the Ex-DC@CQDs group demonstrated a 12.92-fold increase in AUC_{0-∞} compared to free DC, and a 3.6-fold increase compared to DC@CQDs. The average half-life ($t_{1/2}$) of Ex-DC@CQDs was significantly longer, being 16.71 times greater than that of the free drug. Additionally, the mean residence time (MRT) was prolonged, with Ex-DC@CQDs displaying MRT values that were 14.58 times longer than free DC and 2.39 times longer than DC@CQDs, respectively.

These findings strongly support that Ex-DC@CQDs exhibit an extended residence time within the body, potentially leading to improved accumulation at the tumor site through active targeted delivery and the EPR effect. Further, Ex-DC@CQDs demonstrated remarkable targeting efficiency expressed in terms of the Drug Targeting Index (DTI) for Ex-DC@CQDs surpassing both free drugs (17.32%) and DC@CQDs (2.66%) and signifying a pivotal advancement in drug delivery precision. In light of the results, a significant difference was observed in the pharmacokinetic parameters between DC@CQDs and Ex-DC@CQDs. Ex-DC@CQDs were found to have higher AUC, MRT, and $t_{1/2}$ values than DC@CQDs, which can be attributed to the surface morphology, higher biocompatibility, and targeting aspects of Ex-DC@CQDs. Previous reports revealed that nanoparticles with an Exo coating and a target-specific surface decoration demonstrated decreased opsonization properties, which eventually leads to an extended duration of circulation in the bloodstream.

During this study, it was also noted that the DC converts into their active metabolite AIC, which was also supported by previously published articles [Reid *et al* 1999]. The conversion of DC to AIC was also estimated in serum as well as tissue distribution (Figure 7 and Tables 2 and 3) and interestingly it was found that the earlier time points in free DC treated groups showed a higher conversion rate compared to the Ex-DC@CQDs treated group (Figure 7B) which may be ascribed to the fact that DC encapsulated in the formulation would not be available to the liver enzyme. However, at the tumor site, the Ex-DC@CQDs treated groups showed higher AIC concentrations compared to free drug and non-targeted CQDs.

When administered, DC undergoes enzymatic conversion in the liver, resulting in its immediate transformation into AIC. As a consequence of this metabolic process, the C_{max} of free DC is lower in comparison to that of Ex-DC@CQDs. As a matter of fact, Exo isolated from cancer cells possess an enzyme (CYP) in a very high concentration required for the drug conversion into a metabolite. The presence of higher concentrations of AIC in tumor tissue in the Ex-DC@CQDs treated groups suggested that this could be due to the presence of a metabolizing enzyme in Exo, which gets activated after reaching to tumor site and triggering an active metabolite formation. BC cell-derived Exo facilitate the cytochrome enzymes, particularly CYP1A1, CYP1A2, and CYP2E1 (Figure 1K), that activate DC specifically within cancer cells due to the TME and thereby preserve the higher concentration of AIC inside the tumor cells while sparing other cells [Joukhadar *et al* 1999]. Because the above phenomenon requires further investigation, our group is working to reveal the detailed mechanism for cancer cell-isolated Exo-based drug conversion into a metabolite. The above outcome can also be supported by the lower MRT, and half-life of the free DC treated group in contrast to the Ex-DC@CQDs treated group with the rapid distribution of the free drug to the organs and rapid elimination by the kidney, which resulted in the lower concentration in blood.



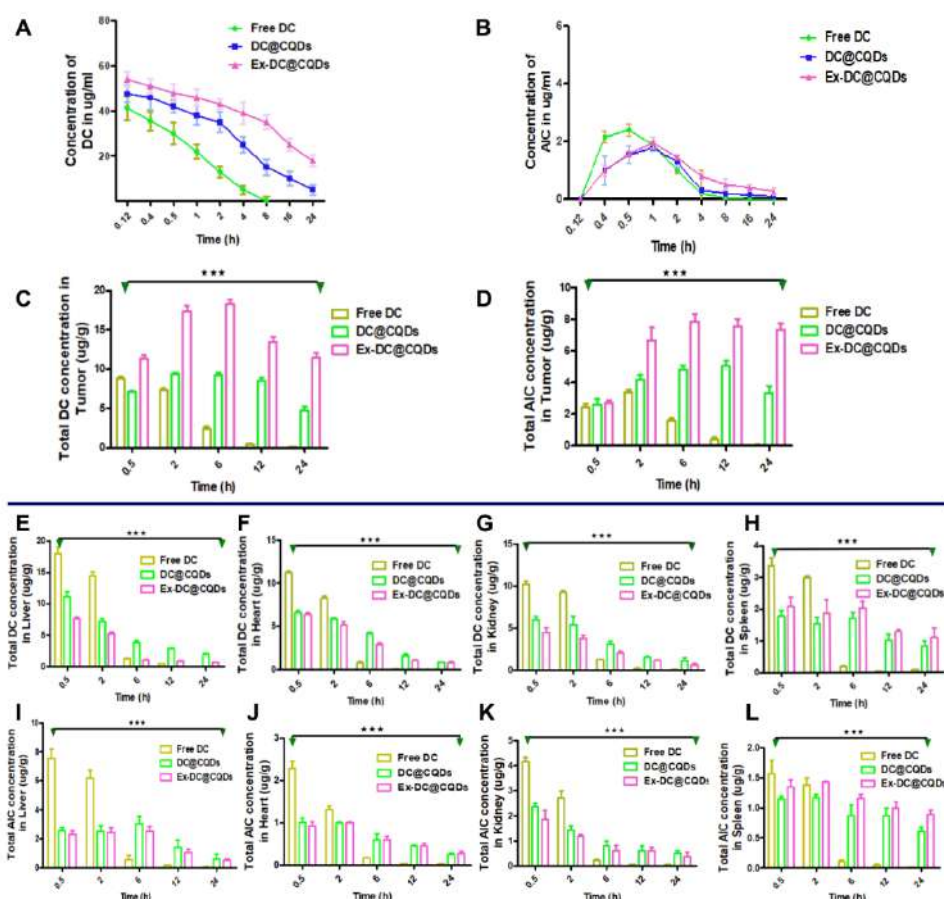


Figure 7. Drug distribution studies in BC mice model after single IV administration of free DC and various formulations. (A-B) Quantitative estimation of DC and metabolite AIC in the serum following IV administration of 10 mg/kg equivalent DC in Free DC, DC@CQDs, and Ex-DC@CQDs treated groups. (C, E-H) Distribution of DC after IV administration of free DC, DC@CQDs, and Ex-DC@CQDs in the tumor, liver, heart, kidney and spleen respectively. (D, I-L) Simultaneously a quantitative analysis was conducted to determine the conversion of metabolite AIC following intravenous administration of Free DC, DC@CQDs, and Ex-DC@CQDs in the tumor, liver, heart, kidney, and spleen respectively. All data are expressed as mean \pm SD (n=6).

Table 2. Pharmacokinetic parameters of DC in mouse serum after single IV administration of Ex-DC@CQDs formulations at a dosage of 10 mg/kg DC. All data are expressed as mean \pm SD (n=6).

Parameter	DC		
	Free DC	DC@CQDs	Ex-DC@CQDs
C_{max} ($\mu\text{g/mL}$)	42.27 \pm 5.21	47.045 \pm 5.41	54.187 \pm 8.11
$t_{1/2}$ (h)	1.01 \pm 1.24	9.21 \pm 1.41	16.88 \pm 1.01
$AUC_{0-\alpha}$ ($\mu\text{g/mL}\cdot\text{h}$)	90.5 \pm 120.34	325.1 \pm 114.12	1169.6 \pm 121.21
V_{ss} ($\mu\text{g/mL}$)	0.174 \pm 0.021	0.322 \pm 0.0045	0.406 \pm 0.022
CI ($\mu\text{g/mL h}^{-1}$)	0.11 \pm 0.0061	0.03 \pm 0.002	8.510 \pm 0.002
MRT (h)	1.646 \pm 1.12	10.05 \pm 3.12	24.003 \pm 3.40

Table 3. Pharmacokinetic parameters of AIC (metabolite) in mouse serum after single IV administration of Ex-DC@CQDs formulations at a dosage of 10 mg/kg DC. All data are expressed as mean \pm SD (n=6).

Parameter	AIC		
	Free DC	DC@CQDs	Ex-DC@CQDs
C_{max} ($\mu\text{g/mL}$)	2.15 \pm 0.25	1.78 \pm 0.11	1.95 \pm 0.24
t_{1/2} (h)	1.408 \pm 0.93	13.79 \pm 0.82	17.99 \pm 0.95
AUC_{0-α} ($\mu\text{g/mL}\cdot\text{h}$)	4.964 \pm 20.34	9.342 \pm 11.02	19.47 \pm 11.01
V_{ss} ($\mu\text{g/mL}$)	4.019 \pm 0.044	13.04 \pm 0.0032	9.512 \pm 0.072
CI ($\mu\text{g/mL h}^{-1}$)	2.015 \pm 0.0033	1.07 \pm 0.004	0.514 \pm 0.001
MRT (h)	1.994 \pm 1.02	15.95 \pm 1.11	21.52 \pm 1.04

In tumor regression study, we investigated the anti-cancer properties of Ex-DC@CQDs using an aggressive 4T1 subcutaneously implanted Balb/c mouse model. After the tumor volume reached 100-110 mm³ in each animal, the mice were segregated into five groups: (I) PBS, (II) CQDs, (III) free DC, (IV) DC@CQDs, and (V) Ex-DC@CQDs. A drug dose equivalent to 10 mg/kg (for DC, DC@CQDs, and Ex-DC@CQDs) was administered IV as a bolus on days 0, 4, 7, 10, 13, 16, and 19 of the study. In order to investigate treatment-driven kinetics behind the cancer progression, tumor burden was measured with a Vernier caliper prior to each administration and calculated as $[\frac{1}{2} \times (L) \times (W)^2]$. The observation revealed that the tumor burden of the Saline treated group increased rapidly within 3 days after injection. On the contrary, the groups that were administered the free drug experienced a slight decrease in tumor growth, likely due to limited bioavailability (Figure 8D). Moreover, the administration of Ex-DC@CQDs exhibited a significantly more potent capability in suppressing the tumor progression, which indicated the enhanced bioavailability of DC as the result of Exo-specific HSPG-mediated targeting. In terms of quantitative analysis, the final tumor volume of Ex-DC@CQDs was found to be significantly lower compared to the control group ($p \leq 0.01$), free DC group ($p \leq 0.01$), and DC@CQDs group. Specifically, the tumor volume of Ex-DC@CQDs was 10.9, 4.8, and 4.3 times lower than in the saline control, free DC, and DC@CQDs groups, respectively. These results provide clear evidence of the superior therapeutic efficacy achieved with the Ex-DC@CQDs and DC@CQDs formulations when compared to the free DC and saline control groups.

Furthermore, at the end of the study, the excised tumor weight in the Ex-DC@CQDs treated group was found to be 7.25-fold, 6.25-fold, and 3.25-fold lower than that of the saline control, free DC, and DC@CQDs groups, respectively. These results align with the findings observed for tumor volume (Figure 8B), indicating a consistent outcome and further supporting the efficacy of Ex-DC@CQDs treatment. The photographic representation of the harvested tumors presented in (Figure 8A) further supports the findings, providing strong corroborating evidence consistent with the in vitro cytotoxicity results. Additionally, in order to assess the safety of the formulations, the body weight of the mice was monitored. As shown in Figure 8C, the group treated with

free DC experienced notable weight loss compared to the other groups. On the other hand, it was observed that the group treated with CQDs alone exhibited both increased efficacy and good tolerability, as indicated by a similar increase in body weight compared to the control group. Therefore, the enhanced antitumor efficacy of Ex-DC@CQDs was attributed to the superior pharmacokinetic profile and higher tumor accumulation resulting from Exo-mediated HSPG receptor-driven cell uptake, as well as the sustained release nature of the carrier-mediated intracellular drug release.

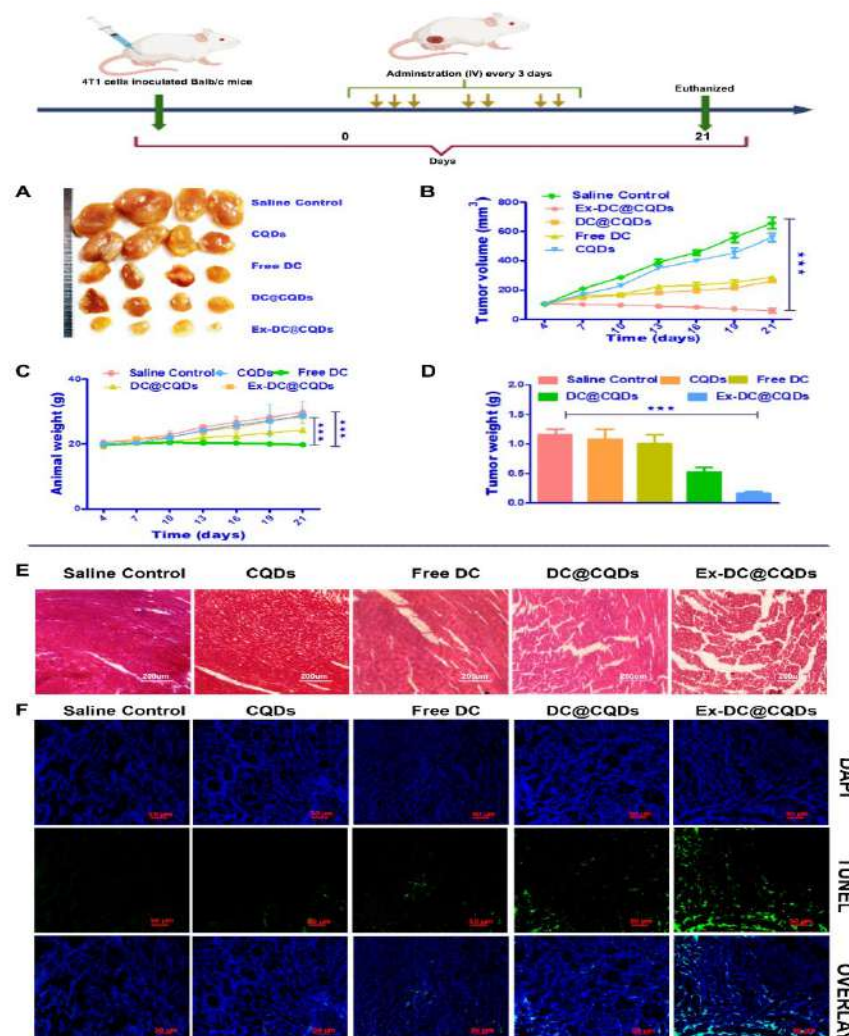


Figure 8. In vivo tumor regression study against 4T1 cells induced mammary tumor in Balb/c mice treated with DC (10 mg/kg). (A) Photographic representation of tumor morphology and shape observed at the end of the study. (B) The mean tumor growth curve at various time points of the study (n=6). (C) The animal body weight monitored during treatment; the results are presented as mean \pm standard deviation (n=6). (D) Weights of excised tumors at the end of the tumor regression study. (E) Histological tumor tissue sections stained with H&E after 21 days of treatment. (F) TUNEL assay of tumor tissue sections from 4T1 tumor associated Balb/c mice treated with different regimens for 21 days. The values are presented as mean \pm standard deviation (n=6).

In this study, we have successfully developed an exosome-derived bioengineered quantum dots-based system to address the issue of complicated imprecise targeting that often leads to clinical toxicity with breast cancer therapy. We devised a strategy that involved loading DC into Fucose-based CQDs, which were then coated with cancer cell isolated Exo, resulting in Ex-DC@CQDs. The studies confirmed the

formation and characteristics of the CQDs and demonstrated that the Exo retained their structural and functional properties within the system. The use of Exo facilitated the targeted delivery of the DC@CQDs to cancer cells through HSPG receptors, thereby enhancing therapeutic efficacy. The study showed that Ex-DC@CQDs exhibited precise targeting and increased cellular uptake, and induced cell death in BC cells through the generation of ROS, depolarization of MMP, and apoptosis. In vivo imaging demonstrated sustained fluorescence intensity at the tumor site, indicating efficient targeting through the exosome-mediated HSPG receptor-driven cell uptake. Additionally, the study evaluated the pharmacokinetic profile and antitumor efficacy of Ex-DC@CQDs compared to free DC and DC@CQDs. The results revealed a significant increase in the AUC_{0-∞} and a substantial reduction in tumor weight in the Ex-DC@CQDs-treated group, indicating improved pharmacokinetics, higher tumor accumulation, and sustained release of the carrier. Overall, our findings feature the potential of exosome-specific targeting and DC@CQD-mediated delivery as an effective intervention for BC. The use of Exo as nanocarriers offers advantages such as precise targeting, enhanced therapeutic efficacy, and reduced toxicity, facilitating the development of a new approach to biologically sourced nanocarriers for cancer targeting.

Journal of Controlled Release 365 (2024) 43–59



Contents lists available at ScienceDirect

Journal of Controlled Release

journal homepage: www.elsevier.com/locate/jconrel



Dacarbazine-primed carbon quantum dots coated with breast cancer cell-derived exosomes for improved breast cancer therapy

Pratiksha Tiwari^{a,c}, Ravi Prakash Shukla^a, Krishna Yadav^a, Neha Singh^a, Disha Marwaha^a, Shalini Gautam^a, Avijit Kumar Bakshi^a, Nikhil Rai^a, Ankit Kumar^a, Deepak Sharma^a, Prabhat Ranjan Mishra^{a,b,*}

J. Controlled Rel. 365 43-59 (2024). (Corresponding author) (I.F. 10.8)

[b] Synchronized Ratio-metric Co-delivery of Metformin and Topotecan through Engineered Mesoporous Silica Nanoparticle Facilitates *in Vivo* Synergistic Precision Levels at Tumor Site [Adv. Healthcare Mater. 7(19):e1800300 (2018)]

Theoretically, the success of combination chemotherapy in cancer majorly depends on the ratios of individual agents at the tumor site. Accounting to the dissimilar pharmacokinetic profiles of individual drugs, meagre penetration, and heterogeneous distribution, the redemption of actual synergistic ratios at the target site confronted issues to realize the ultimate therapeutic effect (Mayer et al 2006). Delivery of synergistic drug ratios through nano-carriers provides controlled, temporal, and spatial delivery of multiple cargos, enables drug accumulation in tumor, and releases the drugs at a synchronized rate, thereby, probability of maintenance of intracellular synergistic drug concentrations is possible (Zhang et al 2016a,b). However, co-encapsulation of multiple drugs with different physicochemical properties in the same nano-carrier and controlling the drug release and to achieve required concentration–time profile at the site of action are always challenging tasks.

To overcome these challenges, we developed a novel hydrophobic ion trapping–assisted loading of **Metformin and Topotecan** using pamoic acid (PA) as *in situ* ion trapping agent. The large surface area of MSNs enables to achieve a high payload of both the drugs and *in situ* ion trapping offers reasonable hydrophobicity to **Metformin**, whereas, **Topotecan** exhibited protagonist for controlling the release. We describe the co-encapsulation of **Metformin and Topotecan** in a lipid bilayer–coated mesoporous silica nanoparticles with an aim to achieve high payload and controlled release profile. To shield the surface silanol groups that are highly lipophilic and known to promote nonspecific binding and mononuclear phagocytic system (MPS) uptake (Zhang et al 2012), the MSNs were camouflaged with lipid bilayer to impart unique attributes which combine the advantages of liposomes with MSNs

A ratio-metric co-delivery platform was developed bearing metformin, a known metabolic modulator and topotecan, a chemotherapeutic drug, by engineering lipid bilayer–camouflaged mesoporous silica nanoparticles that effectively promote apoptosis via mitochondrial membrane depolarization and cell cycle arrest with extended circulation time and higher tumor localization. We developed a novel hydrophobic ion trapping–assisted loading of Metformin (MET) and Topotecan (TPT) using pamoic acid (PA) through ***In Situ Hydrophobic Ion Pairing (HIP)***. The *in vitro* synergy evaluation between MET and TPT using modeling approach is a major highlight of the study, where the derived ratiometric payload of drugs was delivered and evaluated for enhancement of total efficacy of plain drugs in comparison to the mixture of nanoparticles and co-loaded nanoparticles. To develop remote loading procedure, we used PA-loaded LB-MSNs, (PA) LB-MSNs, composed of SoyaPC/cholesterol/1,2- distearoyl-sn-glycero-3-phosphoethanolamine-polyethylene glycol-2000 (DSPE-PEG 2000) at a molar ratio of 7:2.75:0.25 (**Figure 9A**).



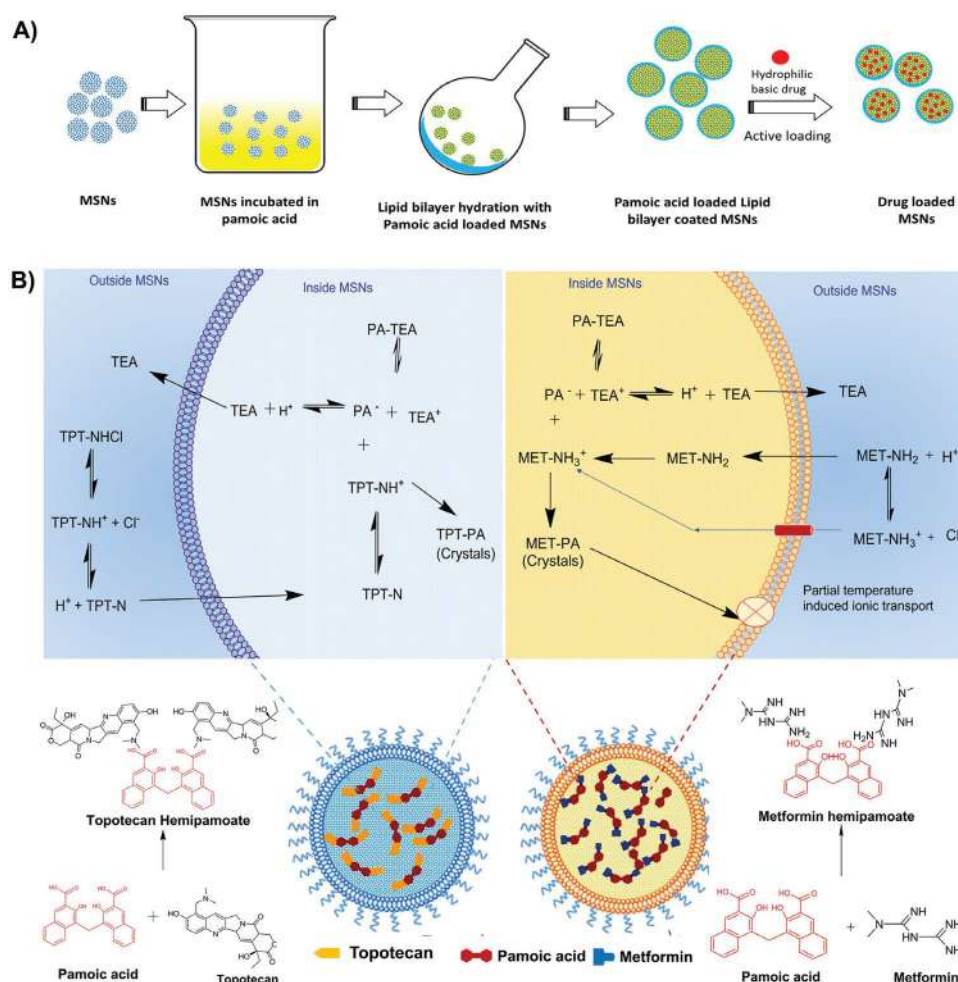


Figure 9. A) Schematics depicting the stepwise preparation of LB-MSNs. B) Mechanistic representation of active loading procedure in PA-loaded LB-MSNs, TEA salt of PA present inside the LB-MSNs allows basic drugs into the MSNs due to gradient difference across the membrane. In case of MET, the higher temperatures partially influence the lipid bilayer permeability. Basic drug after reaching inside MSNs reacts with PA and forms a hydrophobic ion pair (HIP) inside MSN.

Size measurements by DLS technique revealed that the particle size of LB-MSNs was 97.33 ± 5.63 nm, upon loading of PA, the size was slightly increased to 110 ± 8.85 nm (**Figure 10A**). After MTT treatment and obtaining the growth inhibition data, we have used COMBENFIT software package to objectively identify the synergistic combinations of MET and TPT. We assessed the region of the synergy of each combination independently with three established mathematical models, such as Bliss, Loewe, and highest single agent (HSA) models. Based on these modelling data we tried to rationally design the co-loaded LB-MSNs. Initially, we selected six different combinations of MET/TPT. From the MTT assay, it was observed that co-loaded formulations were proven furthermore efficacious compared to a mixture of individual formulations (Figure 11D).

Blue

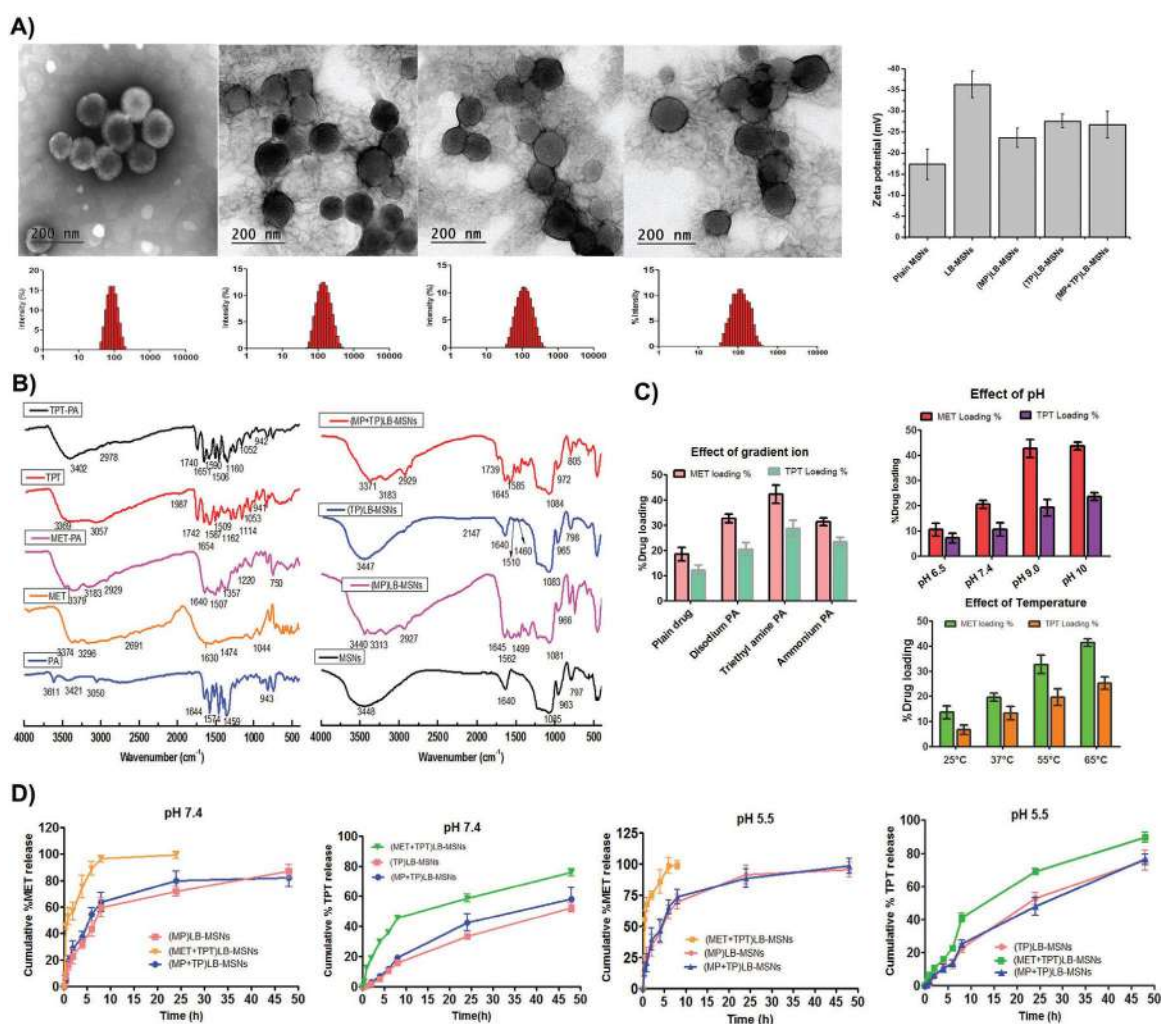


Figure 10. A) Size and polydispersity index (PDI) data of different MSNs, images of transmission electron microscopy (TEM) and dynamic light scattering (DLS) of LB-MSNs, (MP)LB-MSNs, (TP)LB-MSNs, (MP+TP)LB-MSNs (from left to right), and change in zeta potential of different formulations. B) FT-IR of single components (MET, TPT, PA), MET-PA, TPT-PA salts, blank MSNs, and MSNs containing MET, TPT, and PA. C) Various factors affecting the drug loading efficiency; effect of pH, effect of type of gradient ion, and effect of temperature. D) In vitro cumulative percent drug release profiles of MET and TPT from various MSN formulations at pH 7.4 and pH 5.5. All data are expressed as mean \pm SD ($n = 3$).

MSNs loaded with MET and TPT, [(MP) LB-MSNs, (TP) LB-MSNs, and (MP+TP)LB-MSNs] further enhanced the apoptotic effects via mitochondrial membrane depolarization in a synergistic manner. Quantitatively, free MET and TPT induced mitochondrial depolarization in 14.03% and 15.01% cell population, respectively. But, in combination treatment with free drugs slightly enhanced population was observed to be antagonistic. Drug-loaded LB-MSNs significantly enhanced the depolarization representing 27.08% and 31.03% of cell population for (MP) LB-MSNs and (TP) LB-MSNs, respectively. In combination treatment, co-loaded formulation, (MP+TP) LB-MSNs had shown higher depolarization (54.98%) compared to mixture LB-MSNs (42.25%) and Free MET+TPT (20.81%).

Bohe

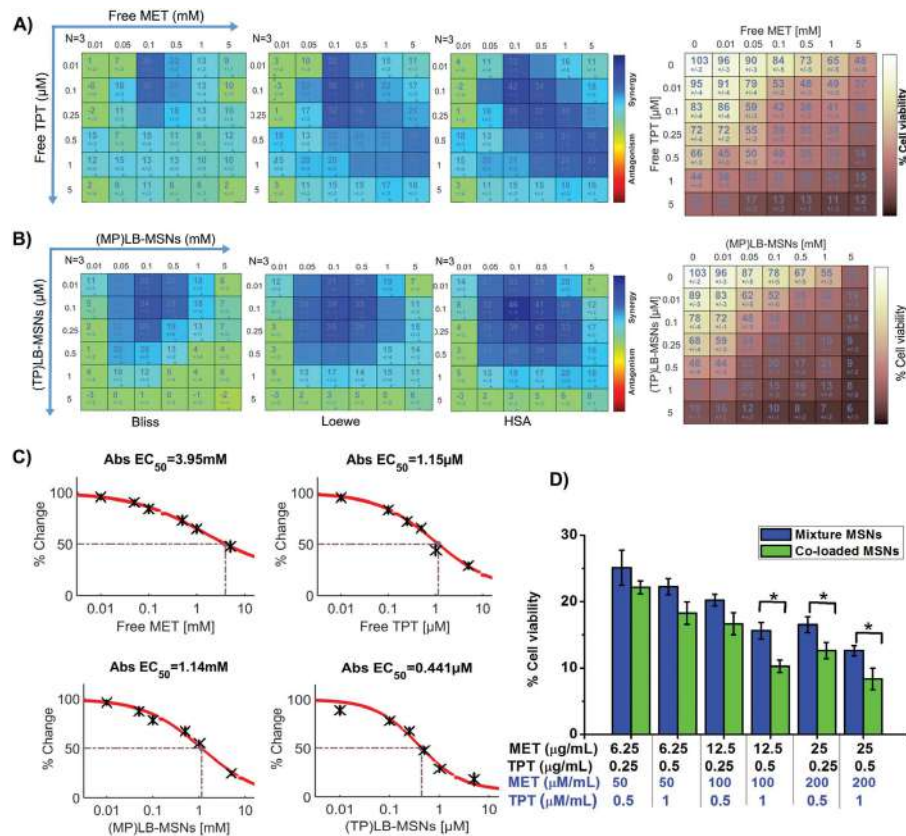


Figure 11. Predicted inhibition data of the three synergy models [Bliss, Loewe, highest single agent (HSA)] in MDA-MB-231 cells treated with A) free MET (x-axis) and free TPT (y-axis), B) (MP)LB-MSNs and (x-axis) and (TP)LB-MSNs (y-axis) in 6 × 6 concentration checkerboard format for 48 h using MTT assay. All data are expressed as mean ± SD, $n = 3$, $*p \leq 0.05$; $**p \leq 0.01$; the synergy spots are represented blue in the matrix and experimental data of growth inhibition compared with control are presented. C) Single-agent effect IC₅₀ of the individual drug and drug-loaded LB-MSNs. D) Comparative growth inhibition data of the co-loaded and mixture formulations in definite ratios. All data are expressed as mean ± SD, $n = 3$, $*p \leq 0.05$.

In order to follow the bio-distribution of the LB-MSNs to the tumor site, animals were intravenously injected with near-infrared (NIR)-labeled (DiR740) LB-MSNs, after achieving the 200–300 mm³ tumor size (**Figure 12A**). IVIS imaging was obtained prior to and following IV injection of 1 mg kg⁻¹ equivalent, DiR-labeled LB-MSNs at the designated time points. Robust fluorescence intensity was observed at the tumor sites within 4 h of LB-MSN injection, following which the signal was sustained for at least 24 h. This was also confirmed by *ex vivo* imaging of the tumors and major organs collected from the animals, following sacrifice 24 h post-injection (Figure 12A1,A2). In addition to abundant particle uptake at the tumor site, the liver and spleen were also major sites of particle distribution. Little signalling was obtained in the lung and kidney. The mixture of solutions (MET+TPT solution) and a mixture of single drug loaded MSNs (MP) LB-MSNs+(TP)LB-MSNs had similar effects.

Bohe

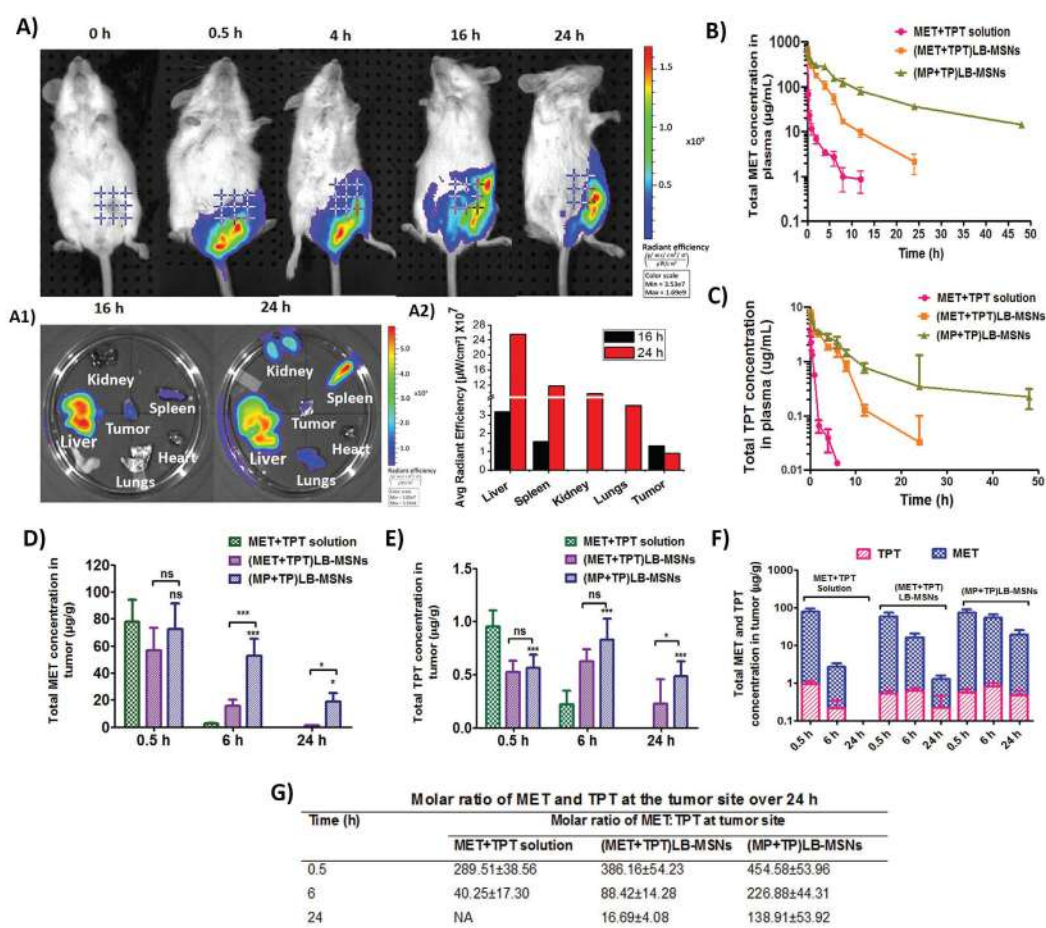


Figure 12. A) Representative IVIS images over 24 h to compare the bio-distribution of i.v. injected DiR-labeled LB-MSNs to the 4T1 tumor-bearing mice and A1) ex vivo biodistribution of explanted organs in the same experiment; animals were sacrificed after 16 h and 24 h. A2) Comparative radiant efficiency in different organs of interest. B,C) MET and TPT concentrations in plasma of different co-loaded LB-MSNs with and without trapping agent (MET and TPT were given a dose of 50 and 1 mg kg⁻¹, respectively). D) Total MET concentration, E) total TPT concentration in tumor tissue with respect to time, all data are expressed as mean ± SD (*n* = 3), statistical significance was determined with one-way ANOVA and differences between groups were determined by Tukey's multiple comparison test, **p* ≤ 0.05; ***p* ≤ 0.01; ****p* ≤ 0.001; ns, nonsignificant. F) Comparison of total MET and TPT tumor accumulation between the MET+TPT solution and different LB-MSN formulations. G) Molar ratio of MET and TPT at tumor site as free or LB-MSN formulations.

Co-loaded (MP+TP) LB-MSNs showed superior antitumor activity than their solutions and the mixture of single drug loaded LB-MSNs with significant differences (*p* ≤ 0.05). The final tumor volume at the end of 20 days post-treatment of co-loaded (MP+TP)LB-MSNs treated group was 13.9-fold, 4.06-fold, and 1.84-fold lower than control, free MET+TPT, and mixture (MP)LB-MSN+(TP) LB-MSN-treated groups, respectively. Whereas, mixture of LB-MSNs had shown 7.5-fold and 2.20-fold lower tumor volumes compared to control and free MET+TPT groups, respectively. The final tumor weight of co-loaded formulation at the end of tumor regression study was 32-fold, 9.69-fold, and 2.29-fold lower than the control group, MET+TPT solution, and mixture(MP)LB-MSN+(TP)LB-MSN group (*p* < 0.001) (Figure 13B).

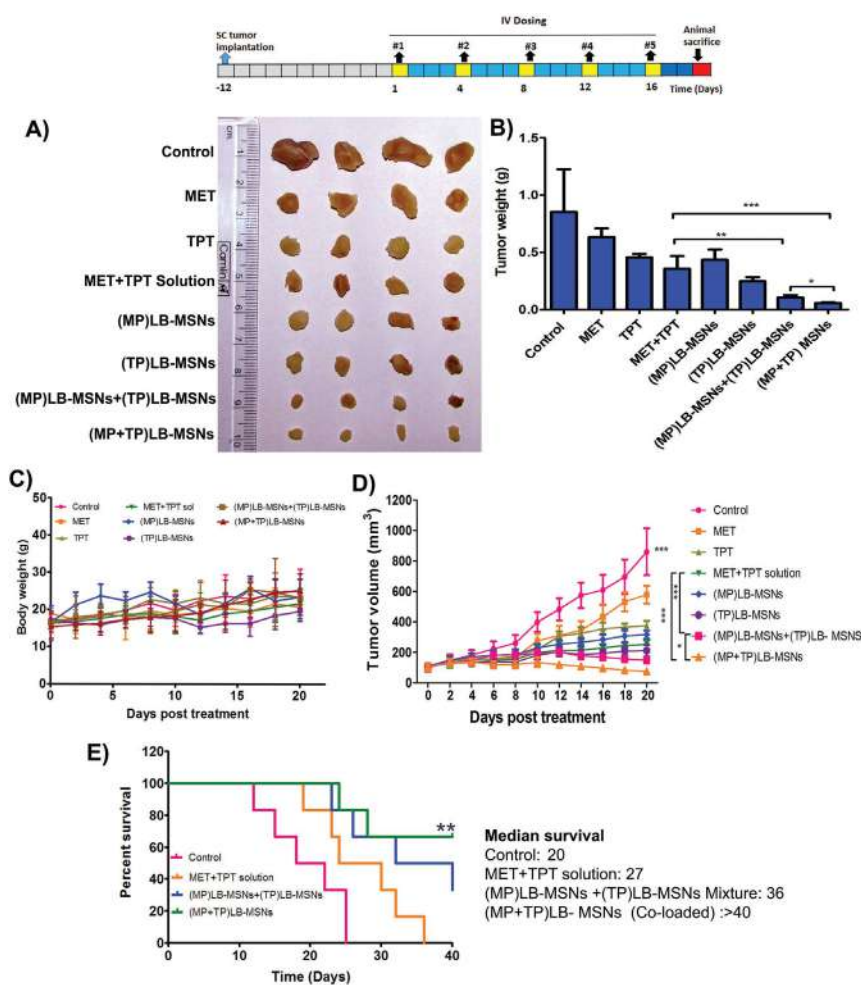


Figure 13. *In vivo* antitumor activity against 4T1 cells transplanted mammary tumor in female BALB/c mice (MET dose: 50 mg kg⁻¹ and TPT dose: 1 mg kg⁻¹ body weight). A) Morphology of the tumors harvested at the end of the study. B) Tumor volume versus time at different time points of the study. All data are expressed as mean \pm SD ($n = 6$), statistical significance was determined with one-way ANOVA analysis. Differences between groups were determined by a Tukey's multiple comparison test, $*p \leq 0.05$; $**p \leq 0.01$; $***p \leq 0.001$; ns, non-significant. C) Body weight changes during the study period. D) Survival rates of 4T1 tumor-bearing mice administrated with a MET+TPT solution and MET+TPT-loaded LB-MSNs, survival data were generated by the Kaplan–Meier method, median survival and statistical significance were determined by log-rank test and Mann–Whitney U test, respectively ($n = 6$), $**p \leq 0.01$.

FULL PAPER

Mesoporous Silica Nanoparticles

ADVANCED
HEALTHCARE
MATERIALS
www.advhealthmat.de

Synchronized Ratiometric Codelivery of Metformin and Topotecan through Engineered Nanocarrier Facilitates In Vivo Synergistic Precision Levels at Tumor Site

Venkatesh Teja Banala, Shweta Sharma, Puja Barnwal, Sandeep Urandur, Ravi P. Shukla, Naseer Ahmad, Naresh Mittapelly, Gitu Pandey, Monika Dwivedi, Navodayam Kalleti, Kalyan Mitra, Srikanta Kumar Rath, Ritu Trivedi, and Prabhat Ranjan Mishra*

Adv. Healthcare Mater. 7(19):e1800300 (2018). (Corresponding author)
(I.F. 11.12)

Prabhat Ranjan Mishra

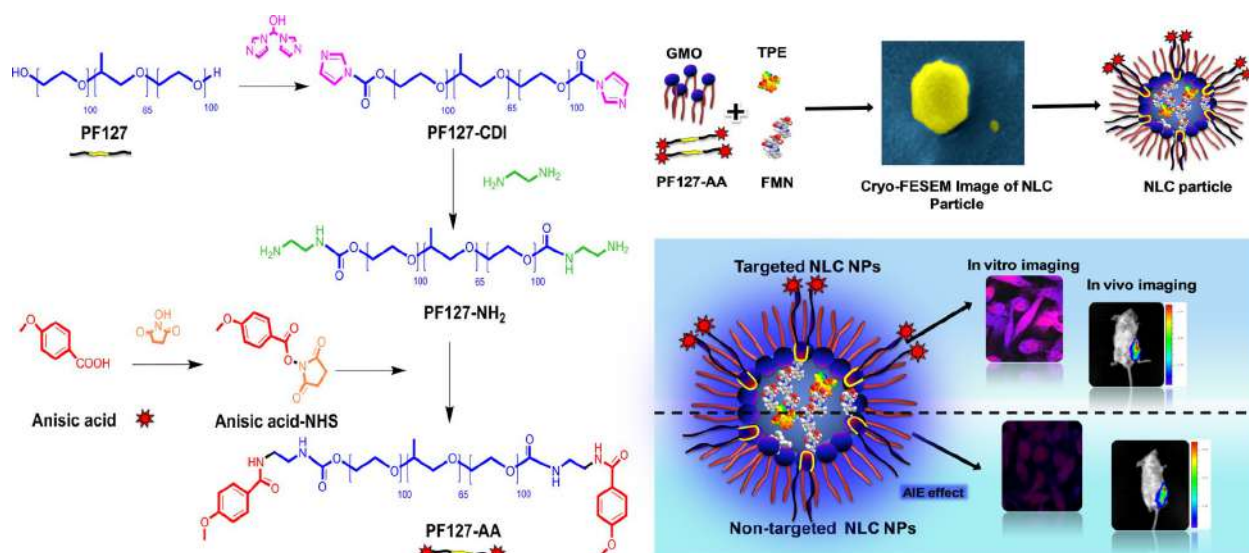
[c] Development and mechanistic elucidation of multimodal nano-theranostic enabling spatial targeting to tumor for imaging and enhanced therapeutic efficacy [ACS Appl. Mater. Interfaces 10(15) 12960-12974 (2018)]

It is the need of hour to have therapeutic strategy with a combination of diagnostic and therapeutic functions into one theranostics systems as an all-in-one approach for better patient compliance. We have elucidated the role of anisamide anchored hexagonal nano-liquid crystals against breast cancer with significantly enhanced efficacy along with non-invasive image-guided chemotherapy through Aggregation Induced Emission (AIE) effect using Tetraphenylethene (TPE) as fluorophores.

We have demonstrated that aggregation-induced emission (AIE) property imparted by Tetraphenylethene (TPE) outperforms the flaws of inorganic contrast agents like small Stokes shift, low photostability, low molar absorptivity and heavy metal cytotoxicity¹. TPE is a propeller-shaped molecule, which, in the dissolved state, possesses torsional motions capable of relaxing the energy of absorbed photons non-radiatively, whereas on aggregation, they promote efficient photoluminescence due to the restriction of their intra-molecular rotations (RIR). It was used to demonstrate that TPE has advantage over conventional organic dyes, which are highly emissive when dissolved, but once clustered in the nanoparticles, aggregation-caused quenching (ACQ) of fluorescence limits the doping amount of dyes, which cannot be swapped by simply increasing the amount of dye concentration. Besides, the unique property to overcome the ACQ effect of conventional organic fluorophores, safety profile along with high “off-on” contrast ratio, large Stokes-shifted fluorescence, long luminescence lifetime, strong photobleaching resistance, and simple and cheap chemical synthesis of TPE-based materials have driven us to select TPE over other AIEgens (Zhu et al 2016; Yu et al 2016).

In this area we have developed an inverse hexagonal (HII) phase liquid crystals for the development of multimodal nanoparticles ensemble of tumor-targeting, imaging and therapeutic properties simultaneously. Initially, we have designed a novel sigma receptor ligand, anisamide (AA)-grafted Pluronic F127 (PF127), using carbodiimide chemistry for the stabilization of glyceryl monooleate (GMO)-based nanoparticles (NLC NPs). Further, the AIE effect was imparted using tetraphenylethene (TPE), an iconic fluorogen in combination with a phytoestrogen, formononetin (FMN), for its spatiotemporal release. For this purpose, GMO-based NLC NPs stabilized by PF127/PF127-AA mixture was loaded with the FMN and TPE (AA-NLC-TF). The synthetic scheme and proposed model illustrating the AIE-based active bio-imaging in vitro and in vivo are shown in Scheme below.





Scheme : Schematic Illustration of Synthetic Steps for PF127-AA and Schematic Illustration of AIE-Based Active Bio-imaging in Vitro and in Vivo

The size of the nanoparticles obtained was suitable for accumulation at the tumor site by enhanced permeability and retention effect as observed with Cryo-FESEM, TEM, and AFM images (Figures 14 and 15). Structural parameters like lattice parameters and water channel radii for AA-NLC-TF is 61.0 ± 0.2 (Å) and 33.1 ± 0.2 r_w (Å) respectively. Inspection of NLC particles through TEM revealed that the particles possessed hexagonal symmetry. Typically, HII phase liquid crystalline particles consist of water-filled continuous cylindrical lipid matrix arranged in the hexagon shape, and as shown in the TEM photo image (Figure 2A). The entrapment efficiencies (EE) of the drug and AIEgen in AA-NLC-TF were found to be 95 and 97%, respectively. Pertaining to measured ζ potential values, they were found to be in the range of -22 to -25 mV. Although GMO, PF127, and PF127-AA do not carry any inherent charge, on the other hand, the negative charge of the nanoparticles could be due to the adsorption of the hydroxide ions of the polarized water layer surrounding its outer surface (Driever et al 2013). As can be seen from the SAXS data (Figure 14B), the Bragg peaks positioned at $1:\sqrt{3}:\sqrt{4}$ ratio represent an HII phase, the targeted nanoparticles (AA-NLC-TF) retained the hexagonal structure.

It was observed that, due to AIE property of TPE trapped in the crystalline core, liquid crystalline particles shows bright blue emission under 365 nm UV light. The presence of AA-NLC-TF nanoparticles in water was also confirmed by shining a laser beam through the nanoparticle solution to observe the Tyndall effect. The absorption and fluorescence emission spectra of AA-NLC-TF were measured. The existence of AIE effect in the nanoparticles was evidenced through the photo-physical studies that advocate the application of NLC NPs in fluorescence-based bio imaging.

Signature

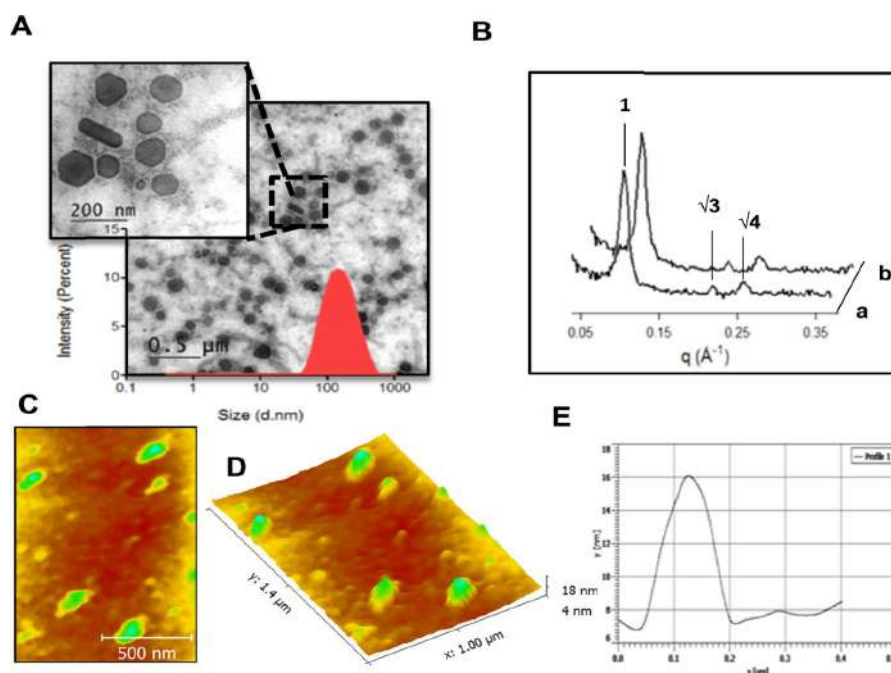


Figure 14: Size and morphological characterization of NLC NPs by (A) TEM (scale bar, 200 nm) and particle size distribution of AA-NLC-TF particles. (B) SAXS intensity plots of (a) blank NLC particles and (b) AA-NLC-TF. AFM images of AA-NLC-TF particles (C) AFM two-dimensional image (scale bar, 500 nm) and (D) 3D view. (E) Height profile.

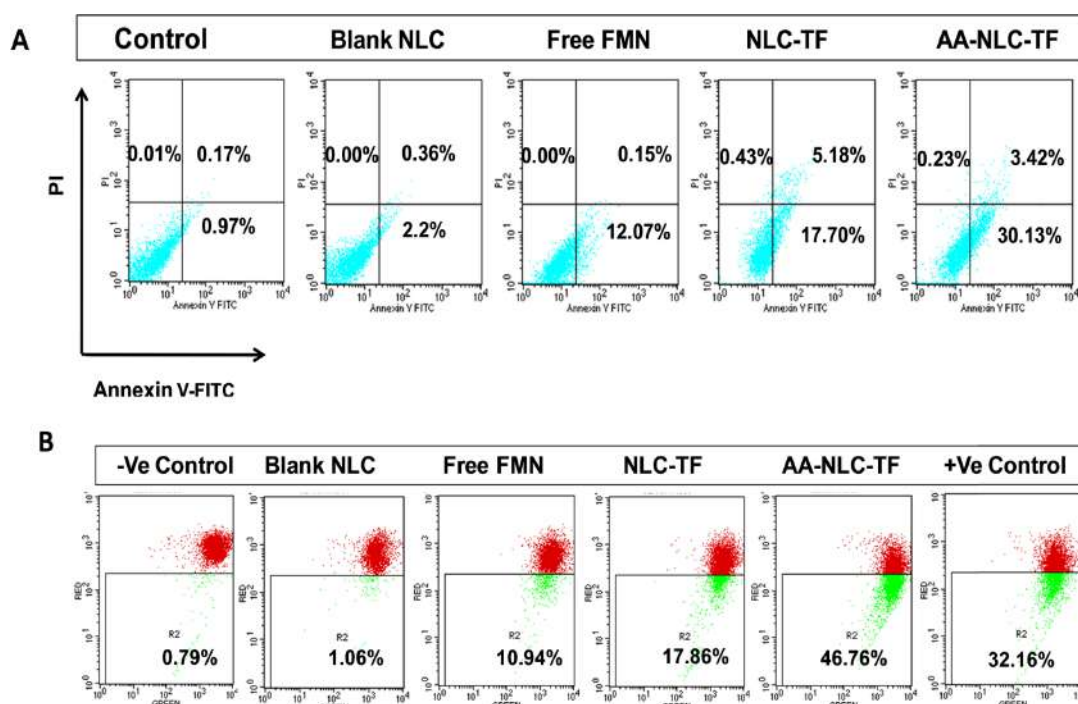


Figure 15: A) Dot plots representing the level of apoptosis in MDA-MB 231 cells after treatment with blank NLC, free FMN, NLC-TF, and AANLC-TF for 48 h. (B) Mitochondrial membrane potential of MDA-MB 231 cells generated after treatment with blank NLC, free FMN, NLC-TF, and AA-NLC-TF for 24 h. PBS-treated cells served as negative control, whereas FCCP-treated cells served as positive control.

Results showed that the apoptotic effect of AA-NLC-TF in MDA-MB 231 cells was more pronounced than free FMN treatment. The apoptotic effect of AA-NLC-TF (33.55%) was higher compared to the apoptotic of NLC-TF (22.88%), free FMN (12.22%), blank NLC (2.56%). As stated previously sigma receptors played a vital role in the uptake of AA-NLC-TF. Reduced apoptotic effects observed after treatment with NLC-TF may be due to its non-targeting property, and findings summarized in the Figure 15A demonstrate the apoptotic effect of treatment regimens and free drug.

Figure 16A, B shows (In vivo imaging) the time dependent tumor accumulation of TPE-loaded nanoparticles in 4T1- cells induced tumor bearing mice when observed using IVIS Kinetic Imaging System. High intense fluorescence was observed after 12 h post-injection of AA-NLCTF when compared to NLC-TF treated group, indicating higher localization of targeted nanoparticles (AA-NLC-TF) in the tumor tissue. The capability of the TPE loaded AA-NLCTF nanoparticles to illuminate the tumor tissue selectively with high contrast may be associated with intense fluorescence of AIE fluorogen -TPE accumulated in the tumor and active tumor targeting ability of the nanoparticles by the AA ligand.

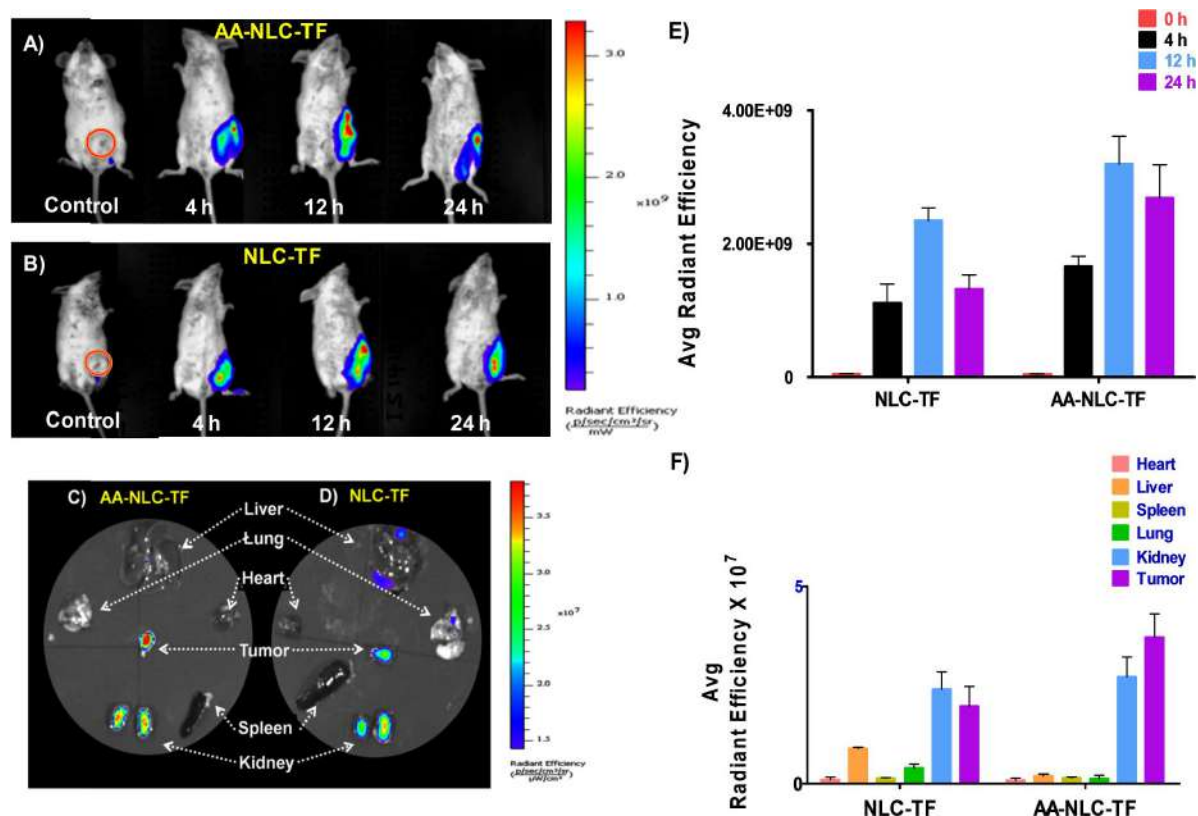


Figure 16: In vivo tumor imaging and tumor-targeting study after iv injection of NLC formulation. (A, B) Body imaging of targeted group and nontargeted group; tumor locations were marked by red circles. (C, D) Ex vivo imaging of major organs from 4T1 tumor-bearing mice at 12 h post injection of the above-mentioned group. (E) In vivo quantification of tumor-associated fluorescence signals of TPE-loaded NLC NPs. (F) Ex vivo quantification of fluorescence signals of TPE-loaded NLC NPs in other major organs. All data are shown as mean \pm SD (n = 3).

Bohe

In vivo antitumor efficacy studies (Figure 17) in 4T1 breast carcinoma transplanted in BALB/c mice (FMN dose: 10 mg/kg body weight) reveals that the average tumor volume of the free FMN treated groups was significantly lower than that of the control group, and the tumor volume of the AA-NLC-TF group was significantly smaller than that of both NLC-TF treated group ($p < 0.001$) and the control group ($p < 0.05$). The results indicated that the active targeting of FMN in NLC-NPs improved its efficacy than free FMN. Compared to control mice, the weight of NLC formulations and free FMN treated mice were remained almost unchanged, these indicate the *in vivo* biocompatibility of the NLC NPs.

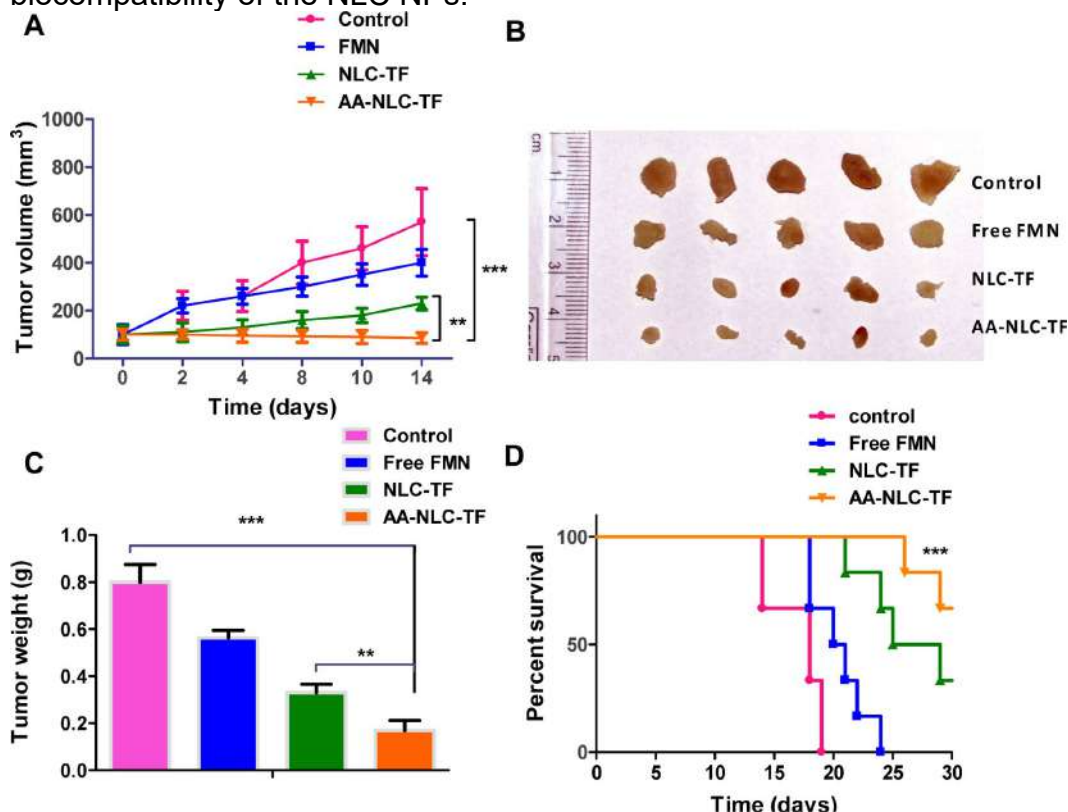


Figure 17: *In vivo* antitumor activity against 4T1 cells transplanted mammary tumor in BALB/c (FMN dose: 10 mg/kg body weight). (A) Tumor volume vs time at different time points of the study ($n = 6$). (B) Morphology of the tumors harvested at the end of the study. (C) Weights of the tumors excised at the end of the tumor regression study. (D) Survival rates of 4T1 tumor-bearing mice ($n = 6$); *** $P < 0.001$ represents control vs AA-NLC-TF, and ** $P < 0.05$ represents NLC-TF vs AA-NLC-TF.)

Publication:

Anisamide-Anchored Lyotropic Nano-Liquid Crystalline Particles with AIE Effect: A Smart Optical Beacon for Tumor Imaging and Therapy

Sandeep Urandur,[†] Venkatesh Teja Banala,[†] Ravi Prakash Shukla,[†] Naresh Mittapelly,[†] Gitu Pandey,[†] Navodayam Kalleti,[‡] Kalyan Mitra,[§] Srikanta Kumar Rath,[‡] Ritu Trivedi,^{||} Pratibha Ramarao,[⊥] and Prabhat Ranjan Mishra^{*,†,§}

ACS Appl. Mater. Interfaces, 10(15) 12960-12974 (2018) (Corresponding author); IF 10.38

[d] Similarly, we also established that, tumor microenvironment can be modulated using **Mn²⁺ functionalized theranostic lyotropic liquid crystalline nanostructures** (LCNs) as a new theranostic arsenal without any external stimulus to achieve advanced comprehensive cancer nano-theranostics. Compared to radiation, photodynamic and photothermal therapy, the selective activation of tumor micro-environmental endogenously for logical generation of cytotoxic OH free radicals serves as an efficient therapeutic strategy for chemodynamic-cancer treatment (Liu et al 2019; Cheng et al 2019). MNPs serves as a fluorescent agent as well as a source of manganese (Mn²⁺) that enables localized oxidative stress under the hallmarks of cancer (acidosis, high H₂O₂ level).

In pursuit of synergistic amplification of Mn²⁺ antitumor activity, Mn-Oleate (MO) complex was synthesized & Fenton catalyst MnO nanoparticles were developed wherein betulinic acid (BA) was loaded in LCN's. In this investigation, nano-architecture of LCN's phase interface is established via SAXS, Cryo-TEM and Cryo-FESEM. Intriguing *in vitro* studies showed that the LCN's triggered hydroxyl radical production and exhibited greater selective cytotoxicity in cancer cells, ensuring safety of normal cells. Significant tumor ablation is realized by 96.5 % of tumor growth inhibition index of LCN's as compared to control group. Key insights into on-site drug release, local anti-cancer response, and tumor location are gained through precise guidance of fluorescent MNPs. In addition, comprehensive assessment of the safety, pharmacokinetics and tumor distribution behavior of LCN's is performed *in vivo* or *ex vivo*. To boost Mn's anti-cancer activity, LCN@Mn-BA was loaded with betulinic acid (2.8 × 10⁻¹ wt%) dependent on the synergistic proportion of Mn and BA obtained from the drug combination experiment. Presence of Mn, O elements was confirmed in the formulation by its unique set of peaks in the electromagnetic emission spectrum (**Urandur et al Acta Biomaterialia 2020**).

Disodium terephthalate (TA) based fluorescence method was used to determine the Fenton-like catalyst activity of LCN@Mn- BA in the presence of H₂O₂, and we explored it by generating OH• radicals under different pH conditions (Fig 18). This work emphasizes the promise of modulating tumor microenvironment with smart endogenous stimuli sensitive nano systems to achieve advanced comprehensive cancer nano-theranostics without any external stimulus. In this investigation, MnO nanoparticles fulfill two needs (fluorescence based optical imaging and a source of Mn²⁺ based chemodynamic therapy) in one unit. This approach also ensures the safety of normal cells, as the toxic OH• free radical activity is substantially suppressed under the mild alkaline/H₂O₂ conditions in normal cell microenvironment.



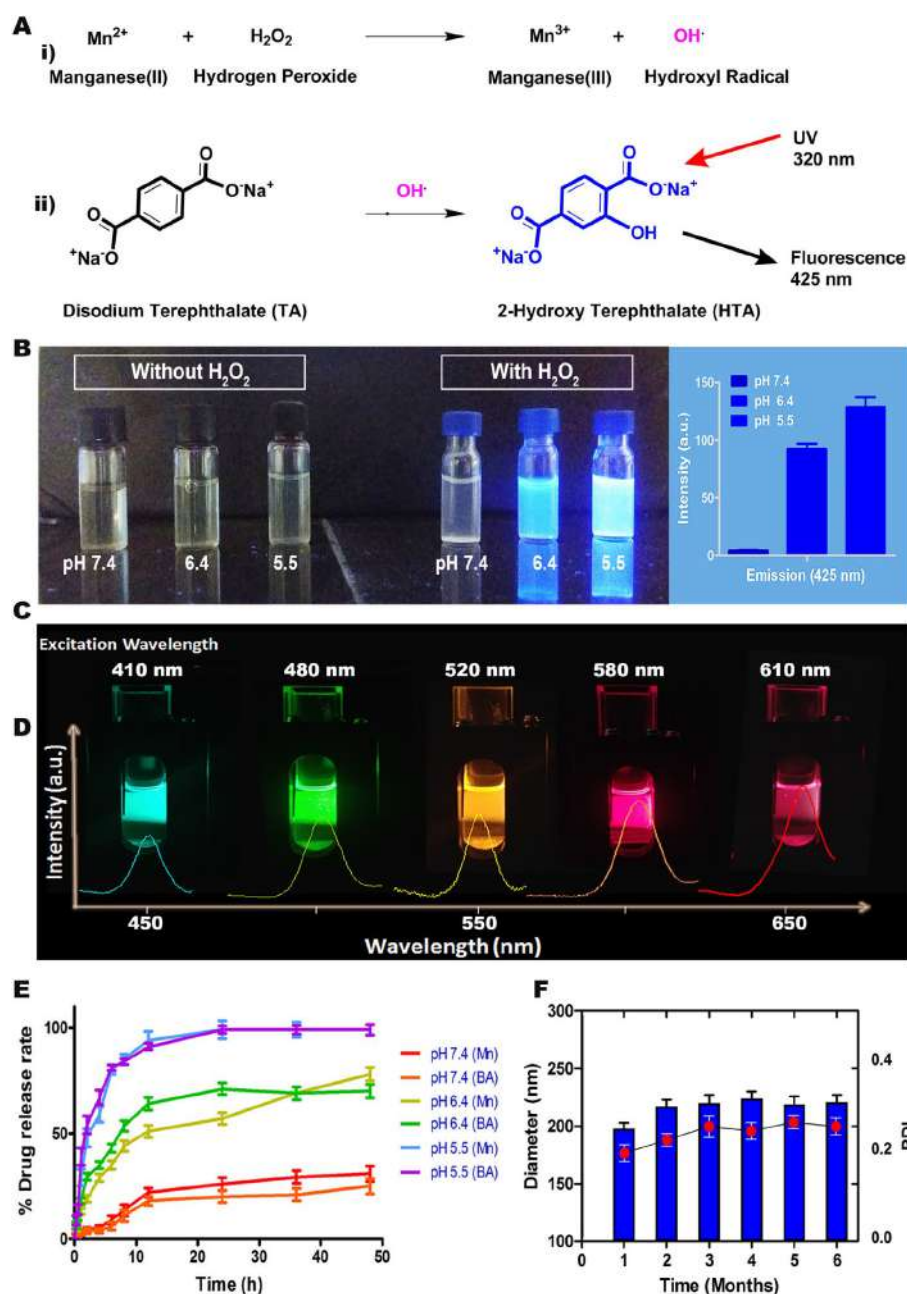


Fig. 18. A) Schematic illustration of i) Fenton like reaction between manganese(II) and hydrogen peroxide generate highly reactive hydroxyl (OH^\bullet) radicals that cause oxidative stress in cancer cells. Disodium terephthalate, a sensitive probe for OH^\bullet radicals was used to detect and to confirm the production of OH^\bullet radicals; (ii) OH^\bullet radicals were detected through the formation of fluorescent 2-hydroxy terephthalate on reaction with disodium terephthalate. B) Digital photographs confirms generation of ROS at different pH without or within the presence of H_2O_2 and fluorescence emission spectra of LCN@Mn-BA at different pH in the presence of H_2O_2 . C) Images showing fluorescence emissions of MNP nanoparticles dispersion at different excitation wavelengths and D) corresponding fluorescence emission spectra. E) *In vitro* drug release profile of LCN@Mn-BA at various pH conditions at 37 °C for 48h. F) Physical stability studies of LCN@Mn-BA conducted in PBS pH 7.4 at 25 °C for six months. All the (E,F) data are expressed in mean \pm S.D, $n = 3$.

The prominent LCN@Mn-BA tumor deposition was also proved using ex-vivo study of excised tumor tissue and other organs. After 24h, high fluorescence intensity was observed in tumor and liver while minimal signals were received from the other

organ such as lungs that might be due to passive accumulation of nanoparticles (Fig. 19 B and D).

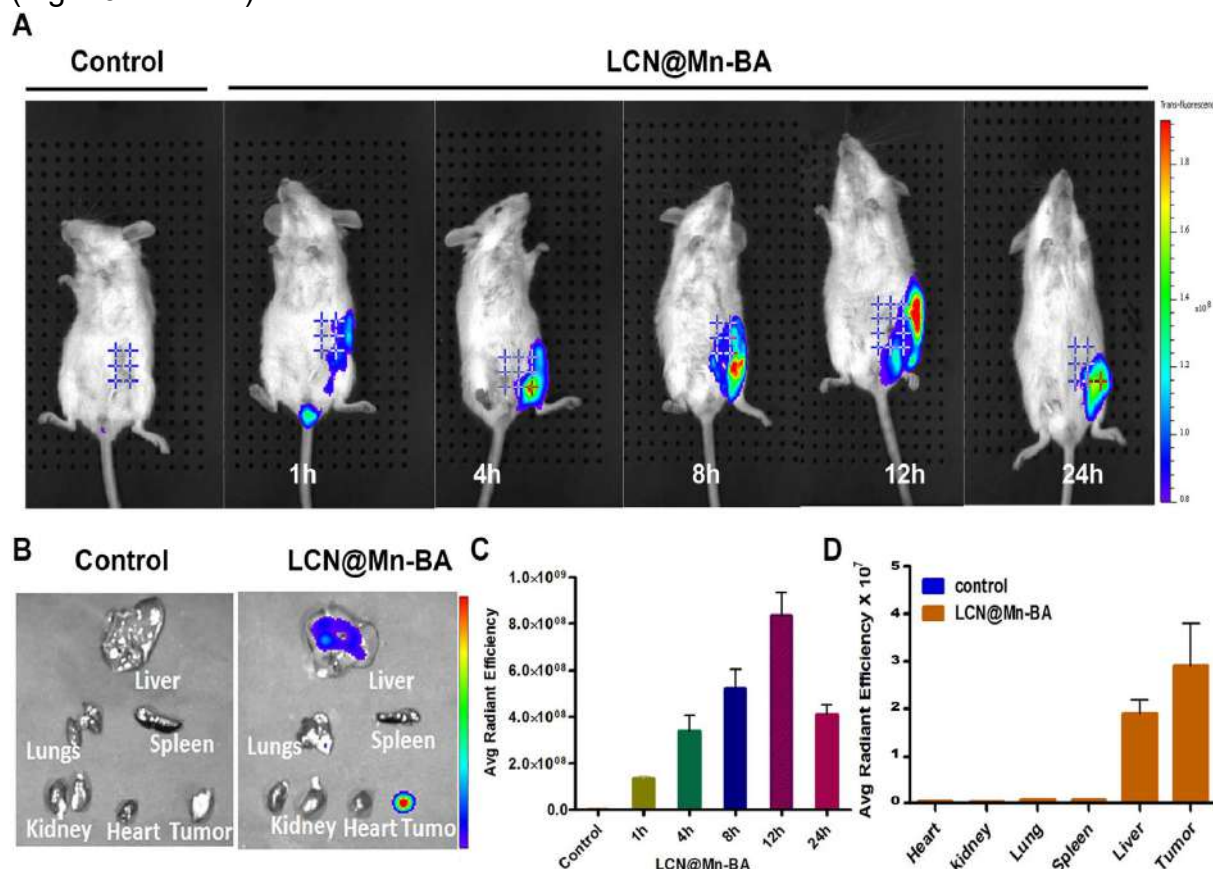


Fig. 19. *In vivo* tumor imaging after i.v. injection of LCN@Mn-BA formulation (1 mg/mL MNP equivalent); A) Body imaging of control and treated group; B) *Ex-vivo* imaging of control and LCN@Mn-BA treated group organs at 24 h of post injection; C, D) *In vivo* quantification of tumor and organs associated fluorescence signals of LCN@Mn-BA nanoparticles.

It was observed that LCN@Mn-BA's anti-tumor efficacy was 6 fold higher than the Mn + BA cocktail and 29 fold higher than control (Fig. 20A). The quantitative tumor growth inhibition index (TIX) rates were 97 ± 3 % for LCN@Mn-BA and 75 ± 4 % for Mn + BA cocktail compared to control. Furthermore, the TIX rate of LCN@Mn-BA was 22 ± 3 times higher than the treatment group for Mn+BA cocktail (Fig. 20B). During this therapeutic period, control group and all therapeutic groups showed no significant variations in body weight indicating no significant toxicity was induced in mice by injection of LCN@Mn-BA, LCN@Mn nanoparticles or free drugs during therapeutic treatment (Fig. 20C). After administration of LCN@Mn-BA nanoparticles, as shown in Fig. 20D mice tumors were dissected and compared to visually demonstrate effective tumor suppression rate. As shown in Fig. 4 E, medial survival time of control, Mn, BA, Mn+BA, LCN@Mn and LCN@Mn-BA was as follows: 25, 27, 32, 40, > 50 days and > 50 days respectively.

Signature

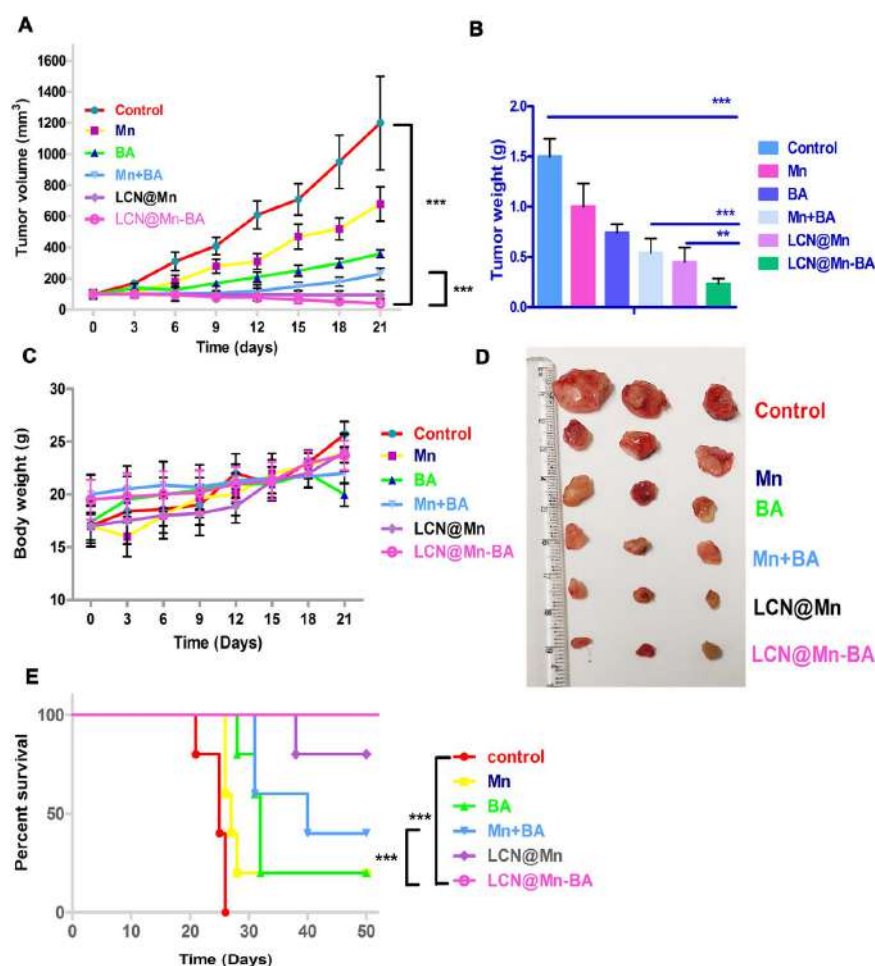


Fig. 20. *In vivo* therapeutic performance of LCN@Mn-BA against 4T1 tumor xenografts. A) tumor volume; B) tumor weight; and C) body weight of 4T1 tumor bearing mice treated with saline (control group), Mn, BA, Mn + BA cocktail, LCN@Mn and LCN@Mn-BA. D) Representative image of tumors dissected at the end of 21 days study. E) The percentage of survival of 4T1 tumor-bearing mice treated with Mn, BA, Mn+BA cocktail, LCN@Mn, LCN@Mn-BA and saline (control group). The data represented as mean \pm SD. The free drugs or LCN's formulation equivalent to dose of 10 mg/kg of BA and 40 mg/kg of Mn were used in the study. * $p < 0.05$, ** $p < 0.01$, *** $p < 0.001$ ($n = 5$ in each treatment group).

Acta Biomaterialia 113 (2020) 522–540



Contents lists available at ScienceDirect

Acta Biomaterialia

journal homepage: www.elsevier.com/locate/actbio



Full length article

Theranostic lyotropic liquid crystalline nanostructures for selective breast cancer imaging and therapy

Sandeep Urandur^a, Venkatesh Teja Banala^a, Ravi Prakash Shukla^a, Shalini Gautam^a, Disha Marwaha^a, Nikhil Rai^a, Madhu Sharma^a, Shweta Sharma^a, Pratibha Ramarao^b, Prabhat Ranjan Mishra^{a,*}

^aPharmaceutics and Pharmacokinetics Division, CSIR-Central Drug Research Institute Lucknow, Sector-10, Jankipuram Extension, Sitapur Road, Lucknow 226031, India

^bSoft Condensed Matter Lab, Raman Research Institute, Bangalore, India

113, 522–540 (2020) (Corresponding author) (I.F. 10.63)

References

- Al-Badr, A.A., Alodhaib, M.M., Dacarbazine, in: Profiles Drug Subst. Excipients Relat. Methodol., 2016: pp. 323–377. <https://doi.org/10.1016/bs.podrm.2015.12.002>.
- Barbouri, D., Afratis, N., Gialeli, C., Vynios, D.H., Theocharis, A.D., Karamanos, N.K., Syndecans as modulators and potential pharmacological targets in cancer progression., *Front. Oncol.* 4 (2014) 4. <https://doi.org/10.3389/fonc.2014.00004>.
- Cheng, Y., Yang, F., Zhang, K., Zhang, Y., Cao, Y., Liu, C., Lu, H., Dong, H., Zhang, X., Non-Fenton-type hydroxyl radical generation and photothermal effect by mito- chondria-targeted WSSe/MnO₂ nanocomposite loaded with isoniazid for syner- gistic anticancer treatment, *Adv. Funct. Mater.* (2019) 1903850
- Choi, Y., Thongsai, N., Chae, A., Jo, S., Kang, E.B., Paoprasert, P., Park, S.Y. I. In, Microwave-assisted synthesis of luminescent and biocompatible lysine-based carbon quantum dots, *J. Ind. Eng. Chem.* 47 (2017) 329–335. <https://doi.org/https://doi.org/10.1016/j.jiec.2016.12.002>.
- Christianson, H.C. Svensson, K.J., van Kuppevelt, T.H., J.-P. Li, M. Belting, Cancer cell exosomes depend on cell-surface heparan sulfate proteoglycans for their internalization and functional activity., *Proc. Natl. Acad. Sci. U. S. A.* 110 (2013) 17380–17385.
- Driever, C. D.; Mulet, X.; Waddington, L. J.; Postma, A.; Thissen, H.; Caruso, F.; Drummond, C. J. Layer-by-layer polymer coating on discrete particles of cubic lyotropic liquid crystalline dispersions (cubosomes). *Langmuir* 2013, 29, 12891–12900.
- exosomes from different sources for cancer-targeted therapy, *Signal Transduct.*
- Gonda, A., Kabagwira, J., Senthil, G.N., Wall, N.R., Internalization of Exosomes through Receptor-Mediated Endocytosis, *Mol. Cancer Res.* 17 (2019) 337–347. <https://doi.org/10.1158/1541-7786.MCR-18-0891>.
- Joukhadar, C., Klein, N., Mader, R.M., Schrolnberger, C., Rizovski, B., Heere-Ress, E., Pehamberger, H., Strauchmann, N., Jansen, B., Müller, M., Penetration of dacarbazine and its active metabolite 5-aminoimidazole-4-carboxamide into cutaneous metastases of human malignant melanoma., *Cancer.* 92 (2001) 2190–2196. [https://doi.org/10.1002/1097-0142\(20011015\)92:8<2190::aid-cnrcr1562>3.0.co;2-2](https://doi.org/10.1002/1097-0142(20011015)92:8<2190::aid-cnrcr1562>3.0.co;2-2).
- Li, S. ,| Su, S., Wu, H., Yuan, T., Yuan, C., Liu, J., Deng, G., Gao, X., Chen, Z., Bao, Y., Yuan, F., Zhou, S., Tan, H., Li, Y., Li, X. , Fan, L., J. Zhu, A.T. Chen, F. Liu, Y. Zhou, M. Li, X. Zhai, J. Zhou, Targeted tumour theranostics in mice via carbon quantum dots structurally mimicking large amino acids, *Nat. Biomed. Eng.* 4 (2020) 704–716. <https://doi.org/10.1038/s41551-020-0540-y>.
- Liu Y., Wu J., Jin, Y., Zhen, W., Wang, Y., Liu, J., Jin, L., Zhang, S., Zhao, Y., Song, S., Yang, Y., Zhang, H. Copper(I) phosphide nanocrystals for in situ self-gen- eration magnetic resonance imaging-guided photothermal-enhanced chemo- dynamic synergetic therapy resisting deep-seated tumor, *Adv. Funct. Mater.* (2019) 1904678.
- Papaioannou, N., Marinovic, A., Yoshizawa, N. A.E. Goode, M. Fay, A. Khlobystov, M.-M. Titirici, A. Sapelkin, Structure and solvents effects on the optical properties of sugar-derived carbon nanodots, *Sci.*
- Rao, L. Yu, G.-T., Meng, Q.-F., Bu, L.-L., Tian, R., Lin, L.-S., Deng, H., Yang, W., Zan, M., Ding, J., Li, A., Xiao, H., Sun, Z.-J., Liu, W., Chen, X. Cancer Cell Membrane-Coated Nanoparticles for Personalized Therapy in Patient-Derived Xenograft Models, *Adv. Funct.*

Mater. 29 (2019) 1905671. <https://doi.org/https://doi.org/10.1002/adfm.201905671>.

Rasmussen, M.K., Pedersen, J.N., Marie, R., Size and surface charge characterization of nanoparticles with a salt gradient, Nat. Commun. 11 (2020) 2337. <https://doi.org/10.1038/s41467-020-15889-3>.

Reid, J.M., Kuffel, M.J., Miller, J.K., Rios, R., Ames, M.M., Metabolic activation of dacarbazine by human cytochromes P450: the role of CYP1A1, CYP1A2, and CYP2E1., Clin. Cancer Res. an Off. J. Am. Assoc. Cancer Res. 5 (1999) 2192–2197.

Rennick, J.J., Johnston, A.P.R., Parton, R.G., Key principles and methods for studying the endocytosis of biological and nanoparticle therapeutics, Nat. Nanotechnol. 16 (2021) 266–276. <https://doi.org/10.1038/s41565-021-00858-8>.

Salunkhe, S., Dheeraj, M., Basak, D., Chitkara, A., Mittal, Surface functionalization of exosomes for target-specific delivery and in vivo imaging & tracking: Strategies and significance, J. Control. Release. 326 (2020) 599–614. <https://doi.org/https://doi.org/10.1016/j.jconrel.2020.07.042>.

Sharifi, M., Cho, W.C., Ansariesfahani, A., Tarharoudi, R., Malekisarvar, H., Sari, S., Bloukh, S.H., Edis, Z., Amin, M., Gleghorn, J.P., Ten Hagen, T.L.M., Falahati, M., An Updated Review on EPR-Based Solid Tumor Targeting Nanocarriers for Cancer Treatment., Cancers (Basel). 14 (2022). <https://doi.org/10.3390/cancers14122868>.

Sun, H., Su, J., Meng, Q., Yin, Q., Chen, L., Gu, W., Zhang, Z., Yu, H., Zhang, P., Wang, S., Li, Y., Cancer Cell Membrane-Coated Gold Nanocages with Hyperthermia-Triggered Drug Release and Homotypic Target Inhibit Growth and Metastasis of Breast Cancer, Adv. Funct. Mater. 27 (2017) 1604300. <https://doi.org/https://doi.org/10.1002/adfm.201604300>.

Tagne, R.N.-B. Compositions and methods for treating cancer with dacarbazine nanoemulsions Target. Ther. 8 (2023) 124. <https://doi.org/10.1038/s41392-023-01382-y>.

V de Medeiros, T., Manioudakis, J. Noun, F., Macairan, J.-R., Victoria, F., Naccache, R. Microwave-assisted synthesis of carbon dots and their applications, J. Mater. Chem. C. 7 (2019) 7175–7195. <https://doi.org/10.1039/C9TC01640F>.

Wang, X., Tian, L., Lu, J., Ng, I.O.-L., Exosomes and cancer - Diagnostic and prognostic biomarkers and therapeutic vehicle, Oncogenesis. 11 (2022) 54. <https://doi.org/10.1038/s41389-022-00431-5>.

Yu, G.; Cook, T. R.; Li, Y.; Yan, X.; Wu, D.; Shao, L.; Shen, J.; Tang, G.; Huang, F.; Chen, X.; Stang, P. J. Tetraphenylethene-based highly emissive metallacage as a component of theranostic supramolecular nanoparticles. Proc. Natl. Acad. Sci. U.S.A. 2016, 113, 13720–13725.

Zeng, Q., Shao, D., He, X., Ren, Z., Ji, W., Shan, C., Qu, S., Li, J., Chen, L., Q. Li, Carbon dots as a trackable drug delivery carrier for localized cancer therapy in vivo, J. Mater. Chem. B. 4 (2016) 5119–5126. <https://doi.org/10.1039/C6TB01259K>.

Zhang, M., Hu, S., Liu, L., Dang, P., Liu, Y., Sun, Z., Qiao, B., Wang, C., Engineered Zhu, Z.; Song, B.; Yuan, J.; Yang, C. Enabling the Triplet of Tetraphenylethene to Sensitize the Excited State of Europium(III) for Protein Detection and Time-Resolved Luminescence Imaging. Adv. Sci. 2016, 3, No. 1600146.



[B] TRANSLATIONAL CONTRIBUTION AND COMMERCIALIZATION

We have successfully developed layer-by-layer (LBL) and SMEDDS technology that impacted product development in the area of bone-related disorders. We have been instrumental in patenting 25 technologies, out of which FIVE have been licensed to Industries while TWO are commercialized as Joint Fresh™ and Reunion™ [(Granted US patent 8,496,964; AU Patent; 2010217238A; EP patent 2400957 B1) Other products for the treatment of osteoarthritis and bone loss are also developed (Granted US Patent 10,596,115; AU Patent 2014291615; US patent 10265297)]. In addition, he has been actively involved in developing Umifenovir and its formulation under repurposing for COVID patients whose Phase III clinical trial has been completed.

Technologies Commercialized - 02 (TWO)

(i) Development of Nanoemulsion pre-concentrate comprising Standardized Extract of *Spinacea oleracea* (bearing two potential biomarkers K007 and K008) for Improved Efficacy in Osteoarthritis

As a part of translational research, a licensed anti-osteoarthritic product based on **nanoemulsion pre-concentrate** comprising standardized extract of *Spinacea oleracea*, has been **launched in the market** and is available as **Joint Fresh™** being marketed by **AERAN Labs**. This formulation contains standardized extract with two identified potential biomarkers that has shown remarkable efficacy *in-vitro* but are not bioavailable *in-vivo* after oral administration. Therefore a SMEDDS based formulation was developed that enhanced the bioavailability of biomarkers and dose was reduced to 150 mg/kg from 750 mg/kg. This strategy was patented and finally licensed to Industry and is now commercialized. This is an important step in bringing the benefits to the public at large by developing a product for **osteoarthritis**.



(ii) Reunion™ Tablets containing standardized extract of *Dalbergia Sissoo* for rapid fracture healing

Another Product **Reunion™** available in the market for rapid fracture healing containing standardized extract of *Dalbergia Sissoo* (being marketed by Aeran Labs Pvt. Ltd. This standardized extract contains an active biomarker K024 (Caviunin 7-O-[b-Dapiofuranosyl-(1-6)-b-D-glucopyranoside). As a team member, contributed in estimating K024 biomarker in the tablets and its content uniformity. In addition, has been made to determine and establish the concentration of K024 biomarker in the blood samples of patients and to correlate the biomarker concentration vis-à-vis its efficacy.

